

Tectonothermal Evolution of the Middle Crust in the Trans-Hudson Orogen, Baffin Island, Canada: Evidence from Petrology and Monazite Geochronology of Sillimanite-bearing Migmatites

D. R. Skipton^{1*}, M. R. St-Onge², D. A. Schneider¹ and C. R. M. McFarlane³

¹Department of Earth and Environmental Sciences, University of Ottawa, Ottawa, ON, K1N 6N5, Canada;

²Geological Survey of Canada, Natural Resources Canada, Ottawa, ON, K1A 0E8, Canada and ³Department of Earth Sciences, University of New Brunswick, Fredericton, NB, E3B 5A3, Canada

*Corresponding author. E-mail: dskip037@uottawa.ca

Received June 25, 2015; Accepted July 18, 2016

ABSTRACT

Hall Peninsula, on SE Baffin Island, Canada, exposes a lithologically diverse mid-crustal section of the Paleoproterozoic Trans-Hudson Orogen, which features Paleoproterozoic supracrustal strata overlying Archean crystalline basement. Recent mapping, combined with petrological studies and U–Pb monazite dating, provides new insights into the tectonothermal history of the internal zone of the orogen, as well as mid-crustal orogenic processes in general. Peak metamorphic grade is constrained to progressively increase westward from mid-amphibolite- to granulite-facies conditions and three regional deformation events are recognized: east-directed thin-skinned crustal shortening (D₁); east-vergent, thick-skinned thrusting and folding (D₂); late-orogenic, north–south-directed, thick-skinned folding (D₃). Equilibrium phase diagram modeling constrained by garnet compositional transects in pelite indicates peak mid-amphibolite-facies conditions on the eastern peninsula of ~720–740°C and 6.25–7.25 kbar, followed by cooling and late muscovite growth. In accordance with field evidence for extensive biotite dehydration melting, peak metamorphic conditions of granulite-facies pelite on the western peninsula are estimated at ~810–890°C and ~6.1–7.35 kbar. *In situ* U–Pb monazite geochronology (laser ablation inductively coupled plasma mass spectrometry) constrains the timing of peak metamorphism and concurrent D₁ deformation throughout the peninsula to between c. 1850 and 1825 Ma, coincident with the accretion of crustal blocks and arc terranes during the amalgamation of the orogenic upper plate. A younger population of c. 1800 Ma monazite implies fluid-assisted dissolution–reprecipitation of older monazite, possibly related to the terminal collision of the amalgamated upper plate Churchill domain with the lower plate Superior craton. Combined with published observations, the integrated geochronological and petrological data suggest that the crustal section exposed on Hall Peninsula remained at elevated temperatures (>550°C) for ~100 Myr after the thermal peak. Despite significant crustal thickening and sustained high temperatures, which are comparable with those of large, hot orogens, the crustal section records no evidence of mid-crustal ductile (channel) flow or rapid exhumation during orogenic collapse.

Key words: Trans-Hudson Orogen; P–T–t evolution; equilibrium phase diagram; *in situ* monazite geochronology; LA-ICP-MS

INTRODUCTION

The Trans-Hudson Orogen (THO) is a collisional belt that extends along-strike for ~3000 km from the western USA to Greenland and has a long-lived accretionary and collisional history between c. 1920 and 1800 Ma (Fig. 1; Hoffman, 1988; Lewry & Collerson, 1990). Characterized by significant crustal thickening and high-grade metamorphism, the THO conforms in many ways to the definition of a large, hot orogen (Beaumont *et al.*, 2006). It has been likened to the Himalayan Orogen (St-Onge *et al.*, 2006), and is considered a prototype for modern accretionary processes (Corrigan *et al.*, 2009; St-Onge *et al.*, 2009). The tectonic history of the Quebec–Baffin segment of the THO has been well documented by previous studies (e.g. Lucas, 1989; St-Onge *et al.*, 2007; Corrigan *et al.*, 2009), but tectono-metamorphic investigations of Hall Peninsula (Figs 1 and 2), SE Baffin Island, have been limited by the lack of comprehensive field and geochronological studies. The peninsula provides a well-exposed oblique section of thrust-imbricated supracrustal cover sequences and crystalline basement, and an opportunity to compare mid-crustal tectono-metamorphic processes in the internal zone of the THO with those of similarly large and/or hot orogens. In this contribution, we integrate the results of recent mapping, petrographic studies and mineral analyses, equilibrium phase diagram modeling and *in situ* U–Pb monazite geochronology (laser ablation inductively coupled plasma mass spectrometry; LA-ICP-MS) to decipher the Paleoproterozoic tectono-metamorphic history of the internal zone of the THO. Our results indicate that this segment of the orogen reached peak metamorphism at mid-amphibolite- to granulite-facies conditions under moderate pressures at c. 1850–1825 Ma, with concurrent east-vergent crustal shortening. The data suggest a regional, late-orogenic tectonothermal event at c. 1800 Ma, and together with previous geochronology (Scott, 1999) imply elevated temperatures (>550°C) until c. 1730 Ma. The apparent absence of channel flow and orogenic collapse suggests large-scale rheological or tectonic differences between the THO and similar large and/or hot orogens, which may have implications for understanding the development of these processes.

TECTONIC SETTING

The THO separates the lower plate Superior craton from an upper plate collage of Archean crustal blocks (Churchill plate; Hoffman, 1988; Lewry & Collerson, 1990). The Churchill plate in the Quebec–Baffin segment of the THO (Fig. 2) consists of the Rae craton and several microcontinents that accreted to the Rae margin between c. 1880 and 1840 Ma, prior to the collision of the Churchill plate with the Superior craton at 1820–1795 Ma (St-Onge *et al.*, 2009). The Meta Incognita microcontinent (MIM; Fig. 2), which includes much of

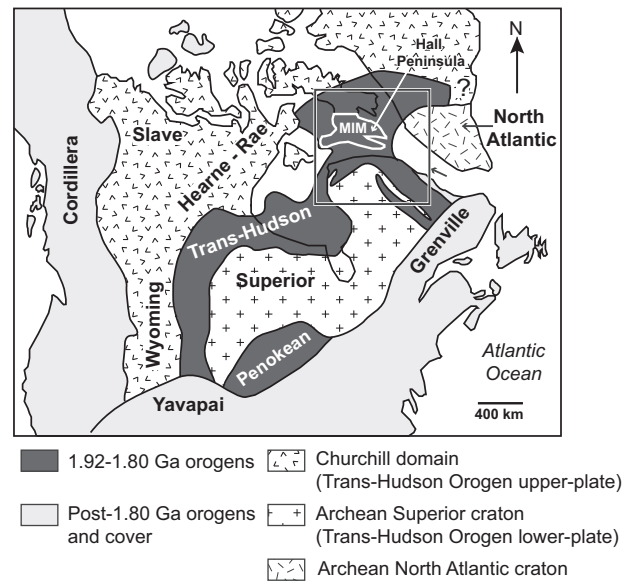


Fig. 1. Simplified tectonic map of North America showing the extent of the Trans-Hudson Orogen, the Superior craton and the Churchill domain, including the Hearne, Rae, Wyoming and Slave cratons. Hall Peninsula on Baffin Island is indicated on the Meta Incognita microcontinent (MIM), outlined in white. Modified after Hoffman (1988) and St-Onge *et al.* (2007).

southern Baffin Island, accreted to the Rae margin between c. 1883 and 1865 Ma (St-Onge *et al.*, 2006). The orthogneissic basement of the MIM is overlain by the Paleoproterozoic Lake Harbour Group, a clastic-carbonate shelf succession, and both basement and cover are intruded by c. 1865–1848 Ma monzogranite to quartz-diorite plutons (Cumberland Batholith; Scott & Wodicka, 1998; St-Onge *et al.*, 2000, 2007; Corrigan *et al.*, 2009; Whalen *et al.*, 2010). Different cratonic origins have been proposed for the basement of the MIM and Hall Peninsula, including the Superior, Rae or North Atlantic craton, the Aasiaat domain in West Greenland, the Core Zone in northern Labrador or a separate cratonic block (Jackson *et al.*, 1990; Scott, 1999; St-Onge *et al.*, 2000, 2009). Several proposed suture zones, when projected, appear to converge on Hall Peninsula, including the east-striking Baffin Suture, the east-striking Disko Bugt and Nagssugtoqidian sutures, and the NW-striking Abloviak Shear Zone (Fig. 2; Corrigan *et al.*, 2009; St-Onge *et al.*, 2009; and references therein).

Granulite-facies metamorphism and fabric development in the MIM at c. 1849–1835 Ma have been attributed to the accretion of the Narsajuaq terrane (Fig. 2) at c. 1845 Ma and Cumberland Batholith magmatism at c. 1865–1848 Ma (St-Onge *et al.*, 2007) or, in a different tectonic model, to the subduction of the Archean crystalline Sugluk Block beneath the MIM along the Big Island Suture (Fig. 2; Corrigan *et al.*, 2009; Whalen *et al.*, 2010). Metamorphic monazite and zircon growth with no associated fabric is also documented in the MIM at c. 1833–1829 Ma (Scott & Gauthier, 1996; Wodicka & Scott, 1997; St-Onge *et al.*, 2007).

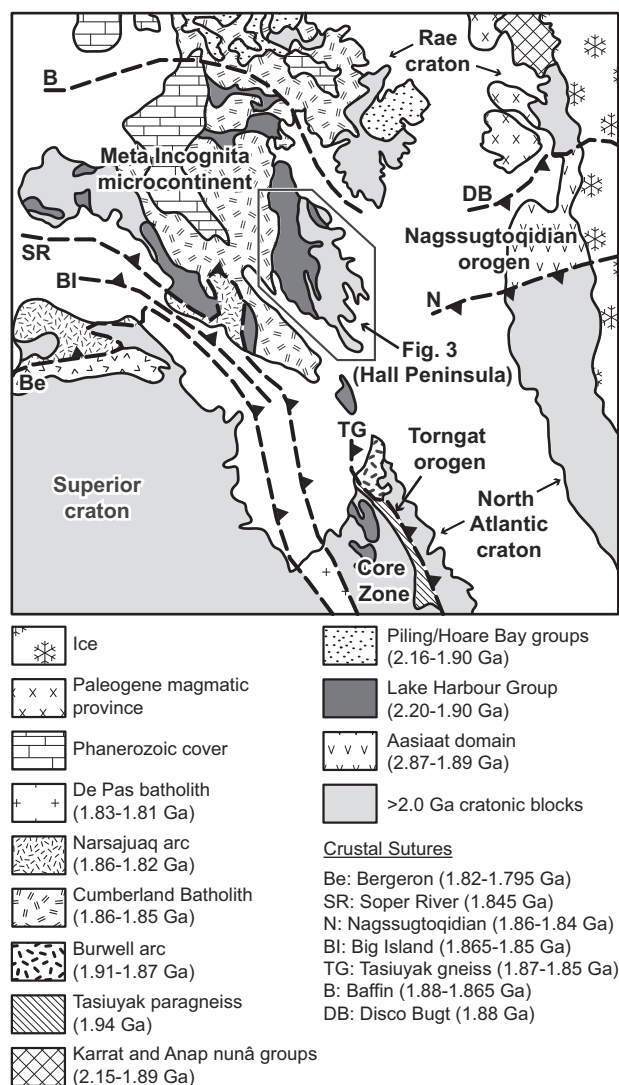


Fig. 2. Generalized geological map of the northeastern portion of the Trans-Hudson Orogen, showing the main lithological units, Archean cratons and crustal sutures proposed by previous studies. Modified after [St-Onge et al. \(2009\)](#).

GEOLOGY OF HALL PENINSULA BASED ON MAPPING (2012–2013)

Lithotypes

Eastern Hall Peninsula is dominated by Archean tonalite and monzogranite gneisses ([Fig. 3](#); [Blackadar, 1967](#); [From et al., 2014](#); [Steenkamp & St-Onge, 2014](#)) ranging from c. 2920 to 2701 Ma in age ([Scott, 1999](#); [Rayner, 2014, 2015](#)). The Archean orthogneisses are unconformably or tectonically overlain or interleaved with supra-crustal sequences of variable thicknesses (10 m to 10 km) ([Machado et al., 2013](#); [Steenkamp & St-Onge, 2014](#)). The cover sequences comprise basal quartzite overlain by interbedded pelite and psammite or inter-layered semi-pelite, meta-calcsilicate, meta-ironstone and amphibolite. The strata have an estimated maximum depositional age of c. 1960 Ma ([Rayner, 2014, 2015](#)). The western peninsula consists of Paleoproterozoic strata and plutonic rocks, with no

exposed Archean basement ([Fig. 3](#)). The western strata comprise psammite, semi-pelite and quartzite, with rare marble horizons ([Machado et al., 2013](#); [Steenkamp & St-Onge, 2014](#)), and have maximum depositional ages of c. 2100–1906 Ma ([Rayner, 2014, 2015](#)). The metasedimentary rocks host leucogranite bodies up to ~100 m thick that contain enclaves of pelite, one of which crystallized at 1867 ± 8 Ma (U–Pb zircon; [Rayner, 2014](#)). The western strata also host orthopyroxene-bearing intrusions, including monzogranite and granodiorite, with lesser diorite and mafic tonalite ([Steenkamp & St-Onge, 2014](#)) that range in age from c. 1890 Ma to c. 1852 Ma ([Scott, 1999](#); [Rayner, 2014, 2015](#)).

Mineral assemblages and metamorphic map

Metamorphic mineral assemblages in pelite were utilized to compile a new metamorphic map for Hall Peninsula ([Supplementary Data Electronic Appendix 1, Fig. A1.1](#); [supplementary data](#) are available for downloading at <http://www.oxfordjournals.org>), combining both field observations and petrography. The mineral assemblages and map document three metamorphic mineral zones that reflect a westward increase in peak metamorphic grade from mid-amphibolite- to granulite-facies. Representative field photographs are provided in [Supplementary Data Electronic Appendix 1 \(Figs A2.1 and A2.2\)](#).

The eastern metamorphic zone is characterized by the mid-amphibolite-facies assemblage biotite + muscovite \pm garnet \pm sillimanite \pm K-feldspar \pm quartzofeldspathic lenses ([Fig. 3](#)). The metamorphic S_1 foliation is defined by aligned biotite, sillimanite, quartzofeldspathic lenses and, in some cases, muscovite. Sillimanite occurs as fibrolite that is surrounded by quartz \pm K-feldspar, forming a faserkiesel texture ([Supplementary Data Electronic Appendix 1, Fig. A2.1a](#)). Muscovite and biotite have similar grain sizes and habits within S_1 . In some localities, muscovite also forms larger grains that cross-cut the S_1 foliation and is interpreted as retrograde and post- D_1 . Discontinuous lenses (≤ 10 cm long) of quartz + plagioclase \pm K-feldspar forming < 15 vol. % are interpreted as crystallized melt, following the criteria of [Sawyer \(1999\)](#). Melt and sillimanite become progressively less abundant towards the east and S_1 -aligned muscovite is more common.

The central metamorphic zone is characterized by the upper amphibolite-facies assemblage biotite + garnet + sillimanite + K-feldspar + quartzofeldspathic lenses and contains no muscovite ([Fig. 3](#)). Whereas sillimanite usually forms fine-grained fibrolite (in faserkiesel clots), it is locally coarse-grained, and quartzofeldspathic lenses, interpreted as former melt, are more voluminous (~10–20 vol. %) ([Supplementary Data Electronic Appendix 1, Fig. A2.1b and c](#)).

The western metamorphic zone features granulite-facies assemblages that include garnet + sillimanite + K-feldspar + quartzofeldspathic lenses \pm cordierite \pm

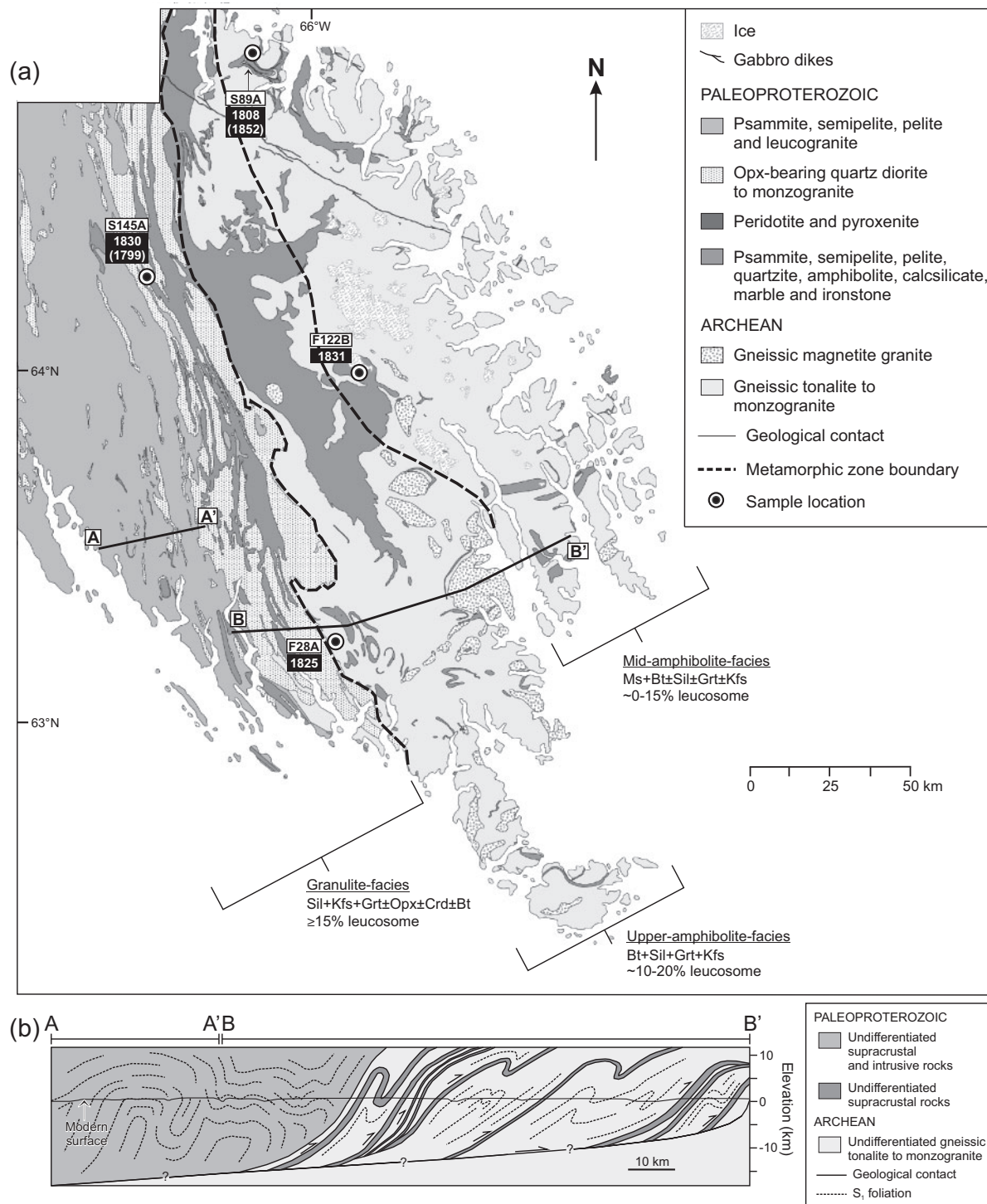


Fig. 3. (a) Generalized lithological map of Hall Peninsula (Fig. 2), modified after Machado *et al.* (2013) and Steenkamp & St-Onge (2014). The map shows sample locations (circles) and the *in situ* U–Pb monazite ages (in Ma) determined in this study within black boxes as dominant age populations and subordinate age populations in parentheses. The three metamorphic zones are outlined (black dashed lines) and labelled with metamorphic grade and characteristic pelitic mineral assemblages. (b) Interpretive cross-section of southern Hall Peninsula through lines A–A' and B–B' in (a). The cross-section was constructed across-strike through a well-exposed portion of southern Hall Peninsula with continuous 1:100 000-scale bedrock mapping along its length and well-constrained lithological and structural relationships. The supracrustal rocks, leucogranite intrusions and monzogranite plutons on the western peninsula are undifferentiated for simplicity and to highlight the overall structure. Archean orthogneisses on the eastern peninsula are undifferentiated. All geological contacts and structures on the cross-section are constrained by surface measurements, and have been projected above and below the surface with an interpreted fault geometry. The principal basement detachment on the cross-section is an interpretation with an assumed depth and geometry.

Table 1: Summary of structural rock fabrics from metamorphic rocks on Hall Peninsula, Baffin Island*

Structural fabric	Description	Mean orientation [†]
<i>D₁: east–west shortening</i>		
F _{1a}	isoclinal folds	AP: 159°/64°; FA: 19–335°
S _{1a}	metamorphic foliation axial planar to F _{1a}	164°/63°
F _{1b}	isoclinal to open folds of S _{1a}	AP: 159°/64°; FA: 19–335°
S _{1b}	metamorphic foliation axial planar to F _{1b}	164°/63°
L _{1a,b}	elongate metamorphic mineral growth	parallel to F _{1a,b} fold hinges, or approximately down-dip
<i>D₂: east–west shortening</i>		
T ₂	thick-skinned reverse faults	SSE-striking, NNE-dipping
L ₂	mineral stretching and elongate growth	30–265°
F ₂	thick-skinned folds, east-vergent	AP: SSE-striking, NNE-dipping; FA: subhorizontal, trending SSE or NNW
<i>D₃: north–south shortening</i>		
F ₃	thick-skinned folds; crenulations	AP: 269°/51°; FA: 37–269°
S ₃	crenulation cleavage axial planar to F ₃	269°/51°

*Fabric orientations are plotted on stereonet in Electronic Appendix 1.

[†]Calculated using GEORient v.9.4.4 (Holcombe, 2009). In plunge-trend notation for linear fabrics and in strike/dip (right-hand rule) notation for planar fabrics; AP is axial plane and FA is fold axis.

orthopyroxene ± biotite (Fig. 3). The S₁ foliation is defined by biotite and compositional banding comprising garnet- and sillimanite-rich bands alternating with quartzofeldspathic bands (Supplementary Data Electronic Appendix 1, Fig. A2.1d–f). K-feldspar, sillimanite and quartzofeldspathic lenses are ubiquitous, and sillimanite is coarse grained. Biotite is scarce and, where present, rims garnet porphyroblasts. Quartzofeldspathic lenses, interpreted as former melt, form ≥15 vol. %, and leucogranite dykes and sills are interpreted as segregated melt (Dyck & St-Onge, 2014). Leucogranite parallel to S₁ contains garnet ± biotite ± cordierite (Supplementary Data Electronic Appendix 1, Fig. A2.1g and h), whereas rare leucogranite dykes that cross-cut S₁ contain muscovite–sillimanite ± garnet (Dyck & St-Onge, 2014). The Paleoproterozoic monzogranite to tonalite intrusions on west-central Hall Peninsula contain biotite–orthopyroxene ± magnetite ± clinopyroxene ± garnet. Some intrusions contain euhedral orthopyroxene phenocrysts and/or euhedral, twinned K-feldspar megacrysts that suggest an igneous origin. However, most of the orthopyroxene is subhedral to anhedral and aligned with the regional metamorphic foliation (S₁), suggesting that it is mostly metamorphic.

Structural geology

Three regional deformation events are recognized: thin-skinned east-directed shortening (D₁); thick-skinned east-directed shortening (D₂); thick-skinned north–south shortening (D₃) (Steenkamp & St-Onge, 2014). These events are summarized in Table 1 and illustrated in Figs 4–6; additional field photographs and stereonet are provided in Supplementary Data Electronic Appendix 1 (Figs A2.1, A2.2 and A3.1). The oldest regional structural elements are east-vergent, isoclinal folds (F_{1a}) of bedding and a west-dipping metamorphic foliation (S_{1a}) that is axial planar to F_{1a} (Fig. 4;

Supplementary Data Electronic Appendix 1, Figs A2.1, A2.2 and A3.1). The S_{1a} foliation is defined by peak mineral assemblages (Figs 5d–h, 6 and 7; Electronic Appendix 1, Figs A2.1 and A2.2). A lineation (L_{1a}) that is parallel to F_{1a} fold axes is defined by elongate mineral growth, including sillimanite on western Hall Peninsula and faserkiesel clots further east (Supplementary Data Electronic Appendix 1, Figs A2.1a and A2.2b). Locally, the D_{1a} fabric has been refolded by east-vergent, isoclinal to open F_{1b} folds with an axial planar S_{1b} foliation and an L_{1b} mineral lineation parallel to F_{1b} fold hinges (Dyck & St-Onge, 2014). The D_{1b} structures have the same orientations as D_{1a} structures, are defined by the same minerals and are indistinguishable without clear field evidence of two fold generations (F_{1a} and F_{1b}). As such, S_{1a} and S_{1b} are treated as equivalent in this study, and both are referred to as S₁. The S₁ foliation planes can contain a lineation defined by elongate or stretched minerals that plunges approximately down-dip (Supplementary Data Electronic Appendix 1, Fig. A3.1), which is interpreted as an L₁ lineation that developed during west-over-east shearing along F₁ fold limbs.

East-directed, basement-involved shortening is evidenced by imbricate thrusts (T₂) on northeastern Hall Peninsula (Figs 3b and 4b), whereby panels of Archean orthogneiss overlie Paleoproterozoic supracrustal rocks (Steenkamp & St-Onge, 2014; Chadwick *et al.*, 2015; Rayner, 2015). Thick-skinned folds (F₂) are associated with T₂ thrusts (Fig. 5a), and the west-over-east kinematics of T₂ and F₂ are shown by rotated porphyroblasts and east-vergent F₂ folds in outcrop. Although 3D exposures of T₂ thrusts and F₂ folds are limited to the east coast, ≤10 km thick panels of Paleoproterozoic supracrustal rocks structurally bounded by Archean orthogneiss occur throughout the eastern peninsula (Steenkamp & St-Onge, 2014).

A west-plunging lineation (L₂) associated with T₂ thrusts and F₂ fold limbs is defined by stretched aggregates of quartz and feldspar (Supplementary Data

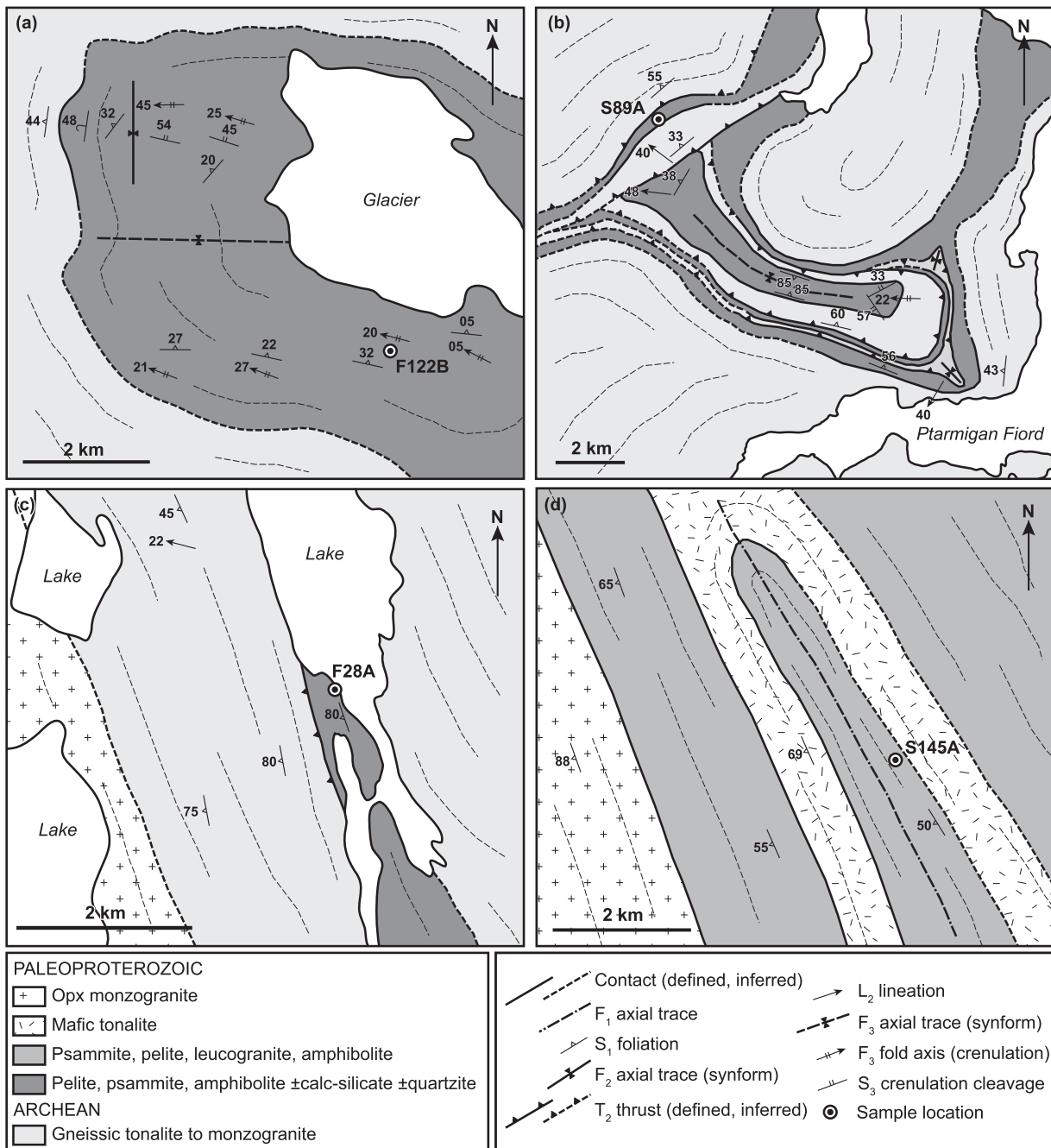


Fig. 4. Detailed geological maps of the sample locations in this study, as indicated in Fig. 3a: (a) F122B; (b) S89A [modified after Chadwick *et al.* (2015)]; (c) F28A; (d) S145A.

Electronic Appendix 1, Fig. A2.2c) (Steenkamp & St-Onge, 2014). With the exception of mylonitization along T_2 thrust contacts (Electronic Appendix 1, Fig. A2.2d–f), the S_1 fabric is preserved and no S_2 metamorphic foliation has been recognized, even in F_2 fold hinges. Given the similarly east-vergent kinematics of D_1 and D_2 , S_2 fabric development cannot be entirely ruled out, but all foliations defined by peak assemblages are designated S_1 in this study.

T_2 thrusting contributed significantly to crustal thickening and to the overall architecture of Hall Peninsula (Fig. 3b). T_2 thrusts juxtapose higher grade

rocks over lower grade rocks, resulting in an inverted metamorphic zonation, suggesting that T_2 thrusting was post-thermal peak on the scale of single thrusts. However, it is also likely that crustal thickening resulting from T_2 thrusting contributed to peak metamorphic conditions in footwall rocks. This is supported by cross-cutting leucogranite in the western granulite-facies zone, as described by Dyck & St-Onge (2014). Cordierite–garnet leucogranite that is interpreted to be a product of biotite dehydration melting is aligned with S_1 , whereas less common muscovite–sillimanite leucogranite, inferred to be the retrograded product of

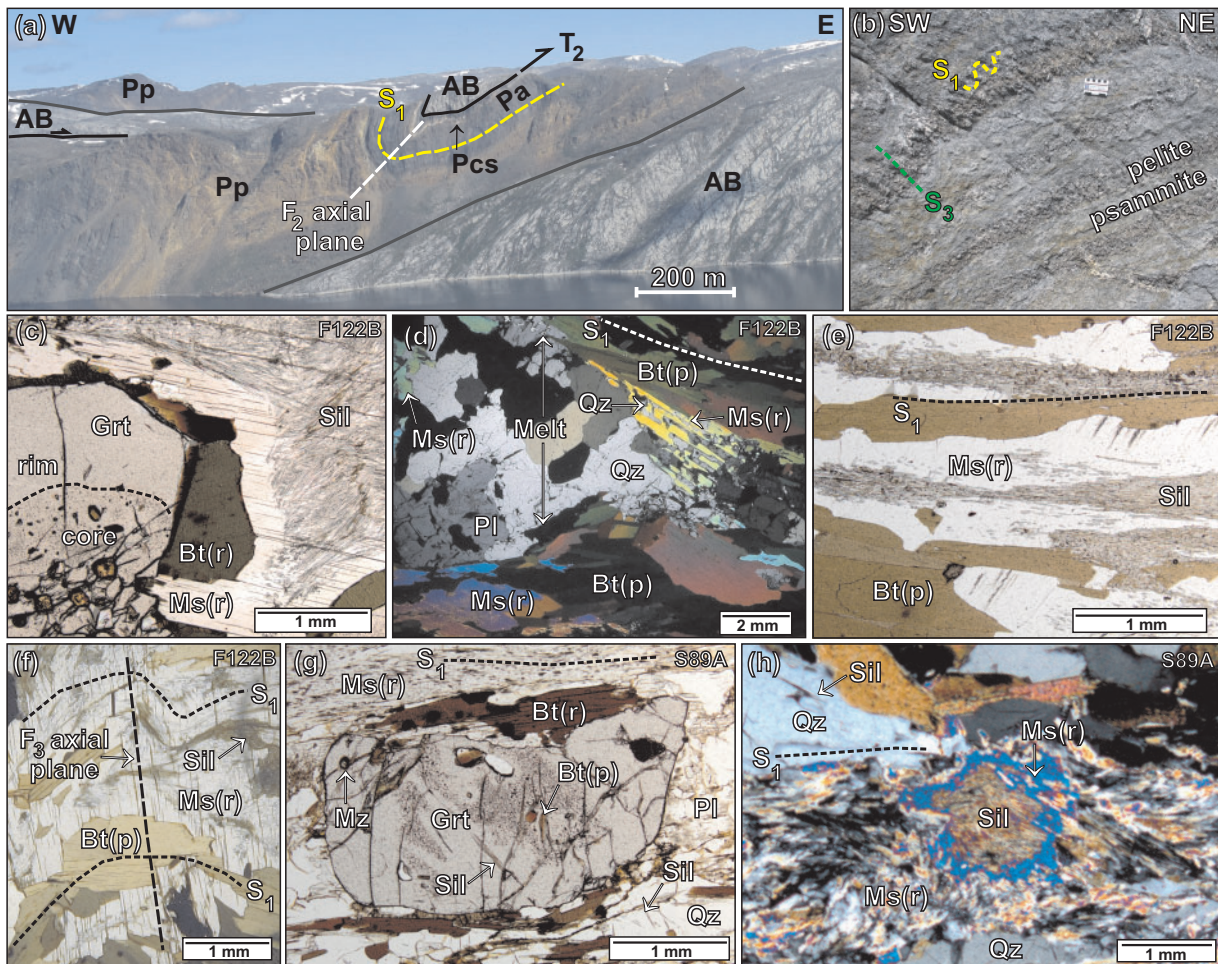


Fig. 5. (a) Photograph of the NE coast of Hall Peninsula, near the location of sample S89A, showing east-directed T₂ thrusting of Archean orthogneiss basement over Paleoproterozoic cover, and F₂ folding of S₁ fabric in cover and basement. AB, Archean basement; Pa, Pp, Pcs, Paleoproterozoic amphibolite, pelite and meta-calc-silicate, respectively. (b) Interbedded pelite and psammite near the location of sample F122B, showing S₁ fabric folded by F₃ crenulations, forming a NNE-dipping crenulation cleavage (S₃). (c–h) Photomicrographs of samples F122B and S89A from thin sections cut perpendicular to S₁ and parallel to L₁, unless otherwise indicated; for micas, ‘(p)’ denotes prograde, syn-D₁ growth whereas ‘(r)’ denotes retrograde, post-D₁ growth. (c) Partially resorbed garnet poikiloblast surrounded by biotite, muscovite and fibrolite. The fibrolite knot is oriented parallel to S₁; however, fibrolite needles are locally at high angles to muscovite cleavage planes [F122B; plane-polarized light (PPL); section is axial planar to F₃]. (d) Band of coarse-grained plagioclase, quartz and rare K-feldspar, interpreted as crystallized melt. Muscovite with symplectic quartz intergrowths in the melt phase may represent retrograde replacement of K-feldspar by muscovite and quartz [F122B; cross-polarized light (XPL); section is axial planar to F₃]. (e) Fibrolite bands in biotite, and overgrown by muscovite that is elongate parallel to S₁ but has cleavage planes oriented axial planar to F₃, suggesting post-S₁ replacement of a pre-existing mineral by muscovite [F122B; PPL; section is axial planar to F₃]. (f) Coarse-grained muscovite overgrows an F₃ crenulation, with muscovite cleavage planes oriented axial planar to F₃ [F122B; PPL; section is perpendicular to the F₃ axial plane]. (g) S₁-aligned garnet poikiloblast surrounded by biotite, plagioclase and quartz. A band of fine-grained muscovite occurs at the top of the photomicrograph, and quartz contains sillimanite needles (S89A; PPL). (h) S₁-aligned band of fine-grained muscovite with quartz. Sillimanite needles occur in quartz and form an aggregate surrounded by a large muscovite crystal at high angle to S₁ (S89A; XPL).

muscovite dehydration melting, cross-cuts S₁ (Dyck & St-Onge, 2014). Consequently, D₂ is interpreted to be broadly syn- to post-thermal peak.

D₁ and D₂ structures are locally folded by post-thermal-peak thick-skinned folds (F₃) up to several kilometres wide with west-striking axial planes. S₁ in pelite is overprinted by centimetre- to decimetre-scale F₃ crenulations and a west-striking crenulation cleavage (S₃; Fig. 5b; Supplementary Data Electronic Appendix 1, Figs A2.2g, h and A3.1) (Skipton & St-Onge, 2014). The geometry of F₃ crenulations implies that D₃ is associated with south-vergent shortening. Rare leucosomes

(Qz + Pl) oriented parallel to S₃ (Supplementary Data Electronic Appendix 1, Fig. A2.2g) suggest that minor melting occurred during D₃ (Skipton & St-Onge, 2014).

Previous metamorphic geochronology

Previous geochronological studies on Hall Peninsula indicate a protracted thermal history, although there is no apparent relation between published U–Pb or Ar ages and their respective location, structural setting or metamorphic grade. The geochronological data are described in detail in Supplementary Data Electronic

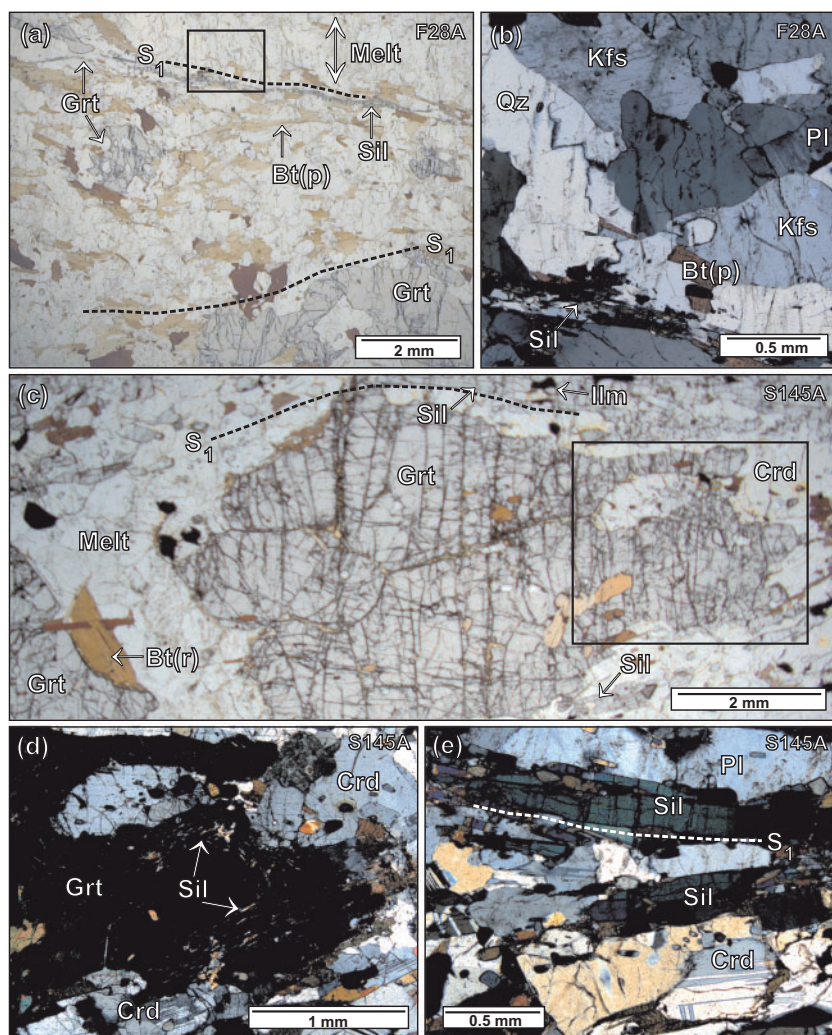


Fig. 6. Photomicrographs of samples F28A and S145A from thin sections cut perpendicular to S_1 and parallel to L_1 ; for micas, '(p)' denotes prograde, syn- D_1 growth whereas '(r)' denotes retrograde, post- D_1 growth. (a) S_1 -aligned compositional banding defined by garnet- and biotite-rich bands alternating with bands of coarse-grained quartz, plagioclase and K-feldspar, interpreted to be melt (F28A; PPL). (b) Detail of area outlined in (a) (F28A; XPL). (c) Elongate garnet, sillimanite, cordierite, ilmenite and minor biotite oriented parallel to S_1 . Coarse-grained quartz, plagioclase and K-feldspar are interpreted as former melt (S145A; PPL). (d) Detail of area outlined in (c), showing a garnet rim containing fine-grained sillimanite needles. Embayments in the garnet rim (top right) suggest replacement of garnet by cordierite (S145A; XPL). (e) Prismatic sillimanite aligned with S_1 , surrounded by cordierite, plagioclase and quartz (S145A; XPL).

Appendix 1. Zircon rims from the three metamorphic zones described above give a range of U–Pb ages from c. 1886 to 1759 Ma (Scott & Gauthier, 1996; Scott, 1999; Rayner, 2014), and U–Pb monazite analyses (isotope dilution thermal ionization mass spectrometry) on four samples from the upper amphibolite- and granulite-facies zones yield ages of c. 1877–1856 Ma (Scott, 1999). A garnet-bearing leucogranite that is interpreted as a melt product of granulite-facies metamorphism crystallized at 1867 ± 8 Ma (U–Pb zircon; Rayner, 2014). Three U–Pb titanite ages range from c. 1742 to 1730 Ma (Scott, 1999) in the mid-amphibolite-facies zone, and ^{40}Ar – ^{39}Ar ages of muscovite from the eastern peninsula range from c. 1690 to 1657 Ma (Skipton *et al.*, 2015). Potassium–Ar ages for minerals from six samples distributed across the peninsula include c. 1700–1507 Ma for biotite (Wanless *et al.*, 1968), c. 1610 Ma for

muscovite (Lowdon, 1960) and c. 1670 Ma for hornblende (Wanless *et al.*, 1979). The age of D_1 deformation is broadly constrained between c. 1873 Ma, the age of a deformed monzogranite dyke, and c. 1830 Ma, the age of an undeformed monzogranite that cross-cuts S_1 (Rayner, 2014, 2015). Minimum ages for D_2 and D_3 have not been determined, as no intrusion cross-cutting D_2 or D_3 structures has been identified.

SAMPLE DESCRIPTIONS AND PETROGRAPHY

The metamorphic history of the THO internal zone on Hall Peninsula was investigated using mineral chemistry, equilibrium phase diagram modeling and *in situ* U–Pb monazite geochronology for four metasedimentary rocks (Table 2; Figs 3 and 4).

Deformation	Prograde D ₁ *	Thermal peak D ₁	D ₂ **	Retrograde syn- to post-D ₃ **
Phase				
Bt				
Ms				
Qz				
Pl				
Kfs				
Grt				
Sil				
Ilm				
Crd				
Melt				
Mnz				
Ttn				
Interpretation	Early D ₁ ; pre- thermal peak	ENE-directed shortening of basement and cover; near-peak, prograde metamorphism and thermal peak	ENE-directed folding and thrusting of basement and cover; syn- to post- thermal peak	S-vergent folding of basement and cover; post-thermal peak

*In Grt inclusion trails in some samples
**dashed lines indicate suspected but unproven relationship

Fig. 7. Summary of mineral–fabric relationships on Hall Peninsula, Baffin Island.

Table 2: Summary of samples from Hall Peninsula, Baffin Island analyzed in this study

Sample	UTM ¹		Rock type	Peak metamorphic assemblage ²	Peak metamorphic grade ³	Structures ⁴
	Easting	Northing				
F122B	656326	7096385	pelite	Bt Sil Qz Pl Grt Kfs Melt*	MA	D ₁ , F ₂ , F ₃
S89A	623387	7195722	pelite	Qz Bt Pl Sil Grt Melt*	MA	D ₁ , T ₂
F28A	649369	7011627	psammite	Qz Pl Kfs Grt Sil Melt†	UA	D ₁ , T ₂
S145A	591234	7127541	pelite	Qz Grt Pl Crd Kfs Sil Ilm Melt†	G	D ₁

¹NAD83 Zone 19 N (Canada).
²Minerals listed from most to least abundant; *contains retrograde (post-D₁) Ms and minor S₁-aligned Ms inferred as prograde;
†contains retrograde (post-D₁) biotite and minor S₁-aligned Bt inferred as prograde
³MA, mid-amphibolite; UA, upper amphibolite; G, granulite.
⁴Refer to Table 1, Fig. 4 and text for details.

Sample F122B: biotite–muscovite–sillimanite–garnet pelite
Sample F122B was collected from a sequence of pelite and psammite that overlies Archean tonalitic gneiss in the eastern mid-amphibolite-facies zone (Fig. 4a). S₁ in the metasedimentary sequence is folded by south-vergent F₃ crenulations (Fig. 5b). Sample F122B comprises biotite, muscovite, sillimanite (fibrolite), garnet (Fig. 5c), plagioclase and quartz. S₁ is defined by aligned biotite, fibrolite, plagioclase and minor muscovite. Plagioclase and quartz are concentrated in ≤1 cm thick bands aligned parallel to S₁ (Fig. 5d), which also contain rare K-feldspar (<2% of sample). Biotite and muscovite grains that define S₁ are medium grained. However, most (~85%) muscovite cross-cuts S₁ and is coarse grained (Fig. 5c–f), including muscovite crystals that engulf fibrolite knots (Fig. 5c, e and f), as well as less common muscovite grains with symplectic quartz intergrowths, located in plagioclase- and quartz-rich bands (Fig. 5d). The post-S₁ muscovite grains that engulf

fibrolite are often, but not always, oriented axial planar to F₃ crenulations (Fig. 5f). Garnet porphyroblasts (~2%) are ≤2 mm wide and are wrapped by S₁. Garnet cores contain inclusions of plagioclase (albite) and biotite, whereas garnet rims are inclusion free and their irregular shape suggests partial resorption (Fig. 5c). Most biotite grains are S₁-aligned, although a later generation of biotite crosscuts S₁, including most grains that are adjacent to resorbed garnet rims.
Leucosome bands of plagioclase–quartz ± K-feldspar that form ~15% of sample F122B are interpreted as former melt, with sillimanite and K-feldspar being the peritectic products of the vapour-absent muscovite dehydration melting reaction (Ms + Pl + Qz = Sil + Kfs + melt; Gardien *et al.*, 1995; Spear *et al.*, 1999; White *et al.*, 2001). Because S₁ is defined by fibrolite bands, plagioclase and leucosome, as well as S₁-aligned muscovite and biotite, S₁ is inferred as syn-thermal peak. Post-S₁ biotite growth probably accompanied partial resorption of garnet rims.

Muscovite aligned with S_1 is interpreted as prograde (e.g. Tyler & Ashworth, 1982). The more abundant muscovite grains that cross-cut S_1 are interpreted as post- D_1 and post-thermal peak. Because this later muscovite occurs as porphyroblasts that engulf fibrolite or as grains with symplectic quartz intergrowths, it is interpreted to have formed through rehydration of K-feldspar following melt crystallization (e.g. Evans & Guidotti, 1966; Ashworth, 1975; Palin *et al.*, 2014). Thus, despite petrographic evidence of muscovite dehydration melting, K-feldspar is rare whereas muscovite is abundant. Because many post- D_1 muscovite grains are axial planar to F_3 crenulations and some crosscut F_3 crenulations, post- D_1 muscovite probably grew as a syn- to post- D_3 phase.

Sample S89A: biotite–muscovite–sillimanite–garnet pelite

Sample S89A, from the mid-amphibolite-facies zone, was collected from an ~500 m thick, NW-dipping supracrustal sequence that is structurally bounded by Archean orthogneiss (Fig. 4b). The strata and their underlying basement form one of several T_2 thrust imbricates mapped on the northern margin of Ptarmigan Fjord (Fig. 4b; Chadwick *et al.*, 2015).

Sample S89A has a NW-dipping S_1 that is defined by bands of fine-grained muscovite \pm sillimanite alternating with bands of coarser grained biotite, muscovite, quartz, plagioclase and garnet (Fig. 5g and h). Muscovite grains in biotite-rich bands are S_1 aligned and medium grained, similar to biotite, and form ~25% of the muscovite in the sample. Within the bands of fine-grained muscovite, many muscovite grains occur at high angles to S_1 (Fig. 5h). Sillimanite (~6%) is present as fine needles in quartz and garnet and infrequently as fine-grained aggregates in muscovite bands (Fig. 5h). Garnet (~2%) forms elongate, S_1 -aligned grains up to 3 mm wide with randomly oriented inclusions of quartz, biotite and sillimanite (Fig. 5g). Garnet grains typically have irregularly shaped rims that are in contact with biotite.

Coarse-grained sillimanite occurs locally in outcrop, as well as in coarse-grained leucogranite dykes that are suggestive of partial melting. The mineral assemblage in sample S89A suggests that it experienced vapour-absent muscovite dehydration melting. However, K-feldspar is absent and only ~5% leucosome occurs in the hand sample. The absence of K-feldspar may be due to the occurrence of large muscovite grains that are not S_1 aligned and surround sillimanite aggregates (Fig. 5h), possibly representing the retrograde replacement of K-feldspar (e.g. Evans & Guidotti, 1966; Ashworth, 1975; Palin *et al.*, 2014). S_1 -aligned bands of muscovite \pm sillimanite (Fig. 5h) are interpreted as retrograde pseudomorphs of sillimanite + quartz \pm K-feldspar (faserkiesel) that grew parallel to S_1 during muscovite breakdown at peak conditions. Minor S_1 -aligned, medium-grained muscovite that occurs with S_1 -aligned biotite may represent prograde muscovite

(e.g. Tyler & Ashworth, 1982). Irregularly shaped garnet rims with adjacent biotite may represent partial resorption of garnet accompanied by late biotite growth (Fig. 5g).

Sample F28A: garnet–sillimanite–K-feldspar psammite

Sample F28A, from the central upper amphibolite-facies zone, was collected from the margin of a 1 km thick, west-dipping package of pelite and psammite that is structurally bounded by tonalite orthogneiss basement; this is ~2 km east of the ~25 km wide belt of orthopyroxene-bearing granitoids on the central peninsula (Figs 3 and 4c). The supracrustal rocks are characterized by a WSW-dipping S_1 fabric and the western contact with the orthogneiss basement is interpreted as a T_2 thrust.

Sample F28A comprises quartz, K-feldspar, plagioclase, garnet, biotite and sillimanite. The S_1 foliation is defined by compositional banding in which bands of coarse-grained quartz (35%), plagioclase (30%) and K-feldspar (35%) alternate with finer grained bands of biotite, garnet and sillimanite (Fig. 6a and b; Supplementary Data Electronic Appendix 1, Fig. A2.1b and c). Biotite (~15%) and sillimanite are S_1 -aligned, and garnet (~4%) forms anhedral, S_1 -aligned porphyroblasts up to 1.5 cm long, as well as a lesser population of smaller, equant grains (Fig. 6a). Garnet contains S_1 -aligned inclusion trails of biotite, plagioclase and quartz.

Bands of coarse-grained quartz, plagioclase and K-feldspar are interpreted as crystallized melt. Based on the presence of leucosome and sillimanite, the abundance of K-feldspar and the absence of muscovite, the sample probably reached temperatures upwards of ~650°C, allowing vapour-absent muscovite dehydration melting and consumption of muscovite. With increased temperatures to ~750°C, biotite dehydration melting may have occurred by the continuous reaction $Bt + Sil + Pl = Grt + Kfs + Sil$ (Spear & Parrish, 1996; Spear *et al.*, 1999). The textures imply that peak metamorphism and partial melting were accompanied by S_1 development.

Sample S145A: garnet–sillimanite–cordierite–K-feldspar pelite

Sample S145A, from the western granulite-facies zone (Fig. 3), was collected from an ~10 km thick sequence of pelite, psammite and quartzite that contains ≤ 1 km thick foliation-parallel intrusions of orthopyroxene tonalite and clinopyroxene gabbro (Fig. 4d). The sequence is folded by F_1 and has a WSW-dipping, axial planar S_1 fabric.

Sample S145A contains garnet, cordierite, sillimanite, quartz, K-feldspar, plagioclase, ilmenite and minor biotite (Fig. 6c–e). S_1 is defined by compositional banding, whereby garnet-, cordierite- and sillimanite-rich bands alternate with bands (~10 vol. %) of coarse-

grained K-feldspar (~35%), plagioclase (25%) and quartz (40%) (Supplementary Data Electronic Appendix 1, Fig. A2.1e and f). S_1 is also defined by aligned garnet, sillimanite, ilmenite, cordierite, quartz, plagioclase and K-feldspar. Garnet (~20% of the rock) forms 3–15 mm wide porphyroblasts that are elongate parallel to S_1 (Fig. 6c). Garnet contains inclusions of biotite and plagioclase; fine sillimanite inclusions are concentrated in the rims of large garnet crystals (Fig. 6d). Sillimanite inclusions are locally oriented parallel to the garnet rim, but are mostly aligned with the S_1 foliation in the matrix. Matrix sillimanite forms prismatic crystals defining S_1 (Fig. 6c). Cordierite generally occurs with garnet and sillimanite, and locally appears to be embaying garnet rims (Fig. 6d). Biotite (~5%) forms S_1 -aligned grains that are concentrated in garnet- and sillimanite-rich bands. A second biotite generation crosscuts S_1 and often occurs adjacent to garnet (Fig. 6c).

Bands of coarse-grained plagioclase, K-feldspar and quartz are interpreted as former melt (e.g. Sawyer, 1999). The mineral assemblage and textures suggest peak conditions at granulite-facies temperatures of at least ~825–850°C, allowing biotite dehydration melting ($Bt + Pl + Qz + Sil = Grt/Crd + Kfs + melt$; LeBreton & Thompson, 1988; Gardien *et al.*, 1995; Spear *et al.*, 1999). The peak mineral assemblage is interpreted as sillimanite, garnet, cordierite, ilmenite, plagioclase, K-feldspar, quartz and melt. Peak metamorphism was probably accompanied by D_1 (Fig. 7), and S_1 probably began to develop during garnet growth and sillimanite nucleation before the thermal peak. Post- S_1 biotite grains embaying garnet rims (Fig. 6c) may reflect the replacement of garnet by biotite during cooling, potentially via the reversal of the biotite dehydration melting reaction. Cordierite located along embayments of garnet (Fig. 6d) may represent replacement of garnet by cordierite during decompression ($Grt + Sil + Qz = Crd$; Bhattacharya, 1993).

MINERAL COMPOSITIONS (MAJOR ELEMENTS)

Analytical methods

Major element analyses were conducted on polished thin sections of each sample using the JEOL JXA-8230 Superprobe at the University of Ottawa (Canada). Analytical methods and a summary of matrix mineral chemistry are given in Supplementary Data Electronic Appendix 1. Representative mineral compositions are given in Supplementary Data Electronic Appendix 2.

Garnet composition

Garnet compositional profiles are shown in Fig. 8; transect locations and compositional maps (Fe, Mg, Mn, Ca, Y) are provided in Supplementary Data Electronic Appendix 1 (Figs A7.1–4). In samples F122B and S89A, garnet rims exhibit decreases in Fe and Mg and increases in Mn and Fe/(Fe + Mg) ratios. Garnet in sample S89A has a relatively homogeneous Ca content,

whereas the garnet core in sample F122B is enriched in Ca relative to rims. In sample F28A, garnet exhibits relatively homogeneous Fe and Mg contents, but there is a slight overall increase in the Fe/(Fe + Mg) ratio towards one garnet rim. The garnet core is slightly enriched in Ca and the Mn content is fairly homogeneous, although there is a small increase in Mn in the rims. In sample S145A, garnet rims have higher Fe/(Fe + Mg) ratios than the garnet cores, particularly where in contact with matrix biotite. The Mn and Ca profiles are relatively flat but show small variations, including slight Mn increases in the rims and near biotite-filled fractures in the garnet interior.

As discussed above, peak mineral assemblages and textural evidence of dehydration melting suggest that all samples reached temperatures upwards of ~650°C. Therefore, any prograde zoning recorded by Fe, Mg and Mn in garnet was probably homogenized in all samples by intra-crystalline volume diffusion, which is effective in garnet at temperatures above ~600°C (Woodsworth, 1977; Florence & Spear, 1991). This explains the fairly flat Fe, Mg and Mn profiles in sample F28A and the Ca and Mn profiles in sample S145A. In samples F122B, S89A and F28A, the relatively flat Ca profiles across garnet imply some homogenization of Ca owing to intra-crystalline diffusion above ~600°C, although garnet cores exhibit slight Ca enrichment compared with rims. This may suggest that prograde, bell-shaped Ca profiles (e.g. St-Onge, 1987; Spear *et al.*, 1990; Florence & Spear, 1993) were incompletely homogenized owing to the slower diffusivity of Ca (Florence & Spear, 1991; Chernoff & Carlson, 1997).

In all samples, increases in Fe/(Fe + Mg) toward garnet rims are attributed to a combination of retrograde net-transfer reactions and retrograde Fe–Mg exchange with adjacent matrix biotite (Kohn & Spear, 2000; Spear, 2004). Strongly elevated Fe/(Fe + Mg) ratios in garnet rims that are in contact with biotite suggest retrograde Fe–Mg exchange between the two minerals, which is also supported by increases in Mg in biotite towards contacts with garnet (Spear, 2004), particularly in samples F28A and S145A. However, Mn-enriched garnet rims and high Fe/(Fe + Mg) ratios in garnet rims that are not in contact with biotite imply that Fe–Mg diffusion with biotite was not the only cause of the high Fe/(Fe + Mg) ratios (e.g. Spear, 2004). In samples F122B and S89A, enrichment of Mn in garnet rims is interpreted as the result of retrograde garnet resorption, possibly by the net-transfer reaction $Grt + Ms = Bt + Pl$, and back-diffusion of Mn into the remaining garnet (Kohn & Spear, 2000). Garnet resorption through retrograde net-transfer reactions is suggested by the non-euhedral shape of the garnet porphyroblasts and irregularly shaped rims (Fig. 5c and g). In samples F28A and S145A, retrograde net-transfer reactions may have occurred via the reversal of biotite dehydration melting reactions during cooling (e.g. Spear, 2004). However, Mn enrichment in garnet rims in samples F28A and S145A is much less pronounced than in lower-grade

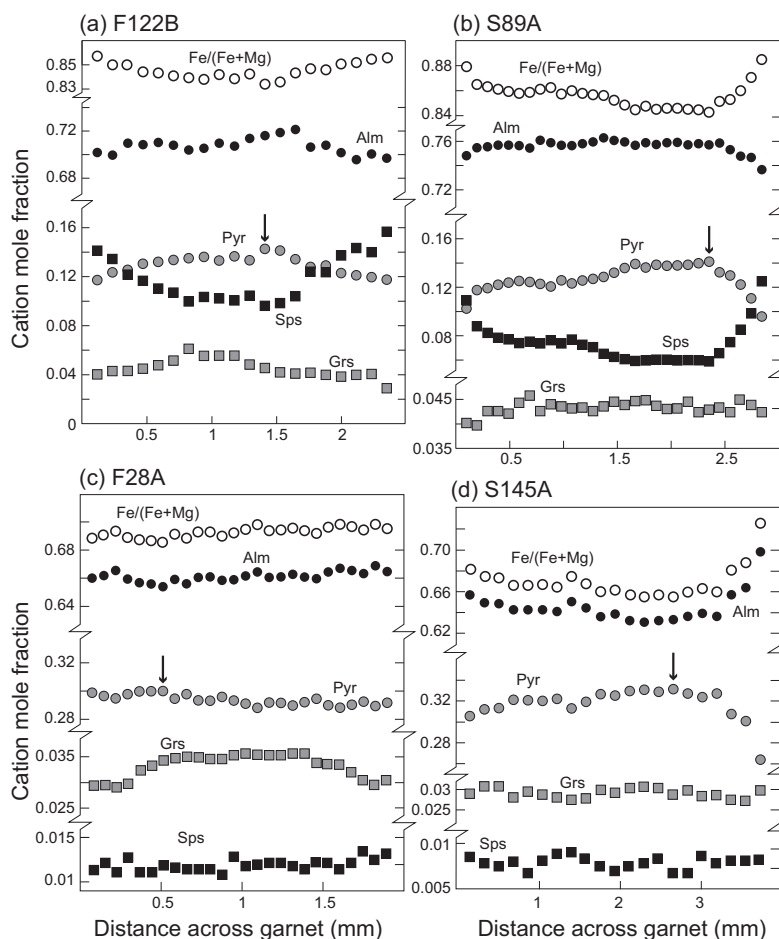


Fig. 8. Compositional transects through garnet porphyroblasts from electron microprobe analyses. Analyses with maximum pyrope values, which are used to estimate P - T conditions at the thermal peak on equilibrium phase diagram models (Figs 9–12), are indicated with arrows. Alm = almandine = $\text{Fe}^{2+}/(\text{Fe}^{2+} + \text{Mg} + \text{Ca} + \text{Mn})$; Pyr = pyrope = $\text{Mg}/(\text{Fe}^{2+} + \text{Mg} + \text{Ca} + \text{Mn})$; Sps = spessartine = $\text{Mn}/(\text{Fe}^{2+} + \text{Mg} + \text{Ca} + \text{Mn})$; Grs = grossular = $\text{Ca}/(\text{Fe}^{2+} + \text{Mg} + \text{Ca} + \text{Mn})$.

samples, despite petrographic evidence of embayed garnet boundaries suggesting retrograde resorption (Fig. 6c and d; Supplementary Data Figs A7.3 and A7.4). This may be attributed to the lower overall X_{Sps} in F28A and S145A and, potentially, because water loss during melting and melt extraction hindered retrograde net-transfer reactions, resulting in lower volumes of resorbed garnet and relatively minor back-diffusion of Mn.

Prograde growth zoning patterns in garnet have been effectively erased owing to compositional homogenization at peak conditions, followed by retrograde Fe–Mg exchange with biotite and retrograde net-transfer reactions. Following the approach of Weller *et al.* (2013) for estimating the composition of homogenized garnet at the thermal peak in sillimanite-grade pelites, the maximum value of pyrope is interpreted to represent the closest approximation of the syn- D_1 peak garnet composition. This composition occurs in the interior of each garnet (arrows in Fig. 8), inboard of rims that are affected by retrograde Fe–Mg exchange or Mn enrichment. However, homogenization of Ca was incomplete in some samples and the degree of

homogenization of Fe, Mg and Mn is uncertain because the ‘peak’ profiles have been modified during cooling. It is also possible that the Mg content of garnet rims during the thermal peak may have been higher than the Mg content of the garnet interior after homogenization. Furthermore, the maximum pyrope composition coincides with slightly elevated X_{Grs} cores in some samples, which may record prograde metamorphism at higher pressures than those of the thermal peak. Despite uncertainties, the maximum pyrope composition is still considered the best possible approximation of the ‘peak’ garnet composition.

PHASE DIAGRAM MODELING

Method

To constrain the stability fields of mineral assemblages from the three metamorphic zones and document the P - T evolution of different pelitic samples, equilibrium phase diagrams were constructed for four samples (F122B, S89A, F28A and S145A) using TheriakDomino v.01.08.09 (De Capitani & Brown, 1987; De Capitani & Petrakakis, 2010; <http://titan.minpet.unibas.ch/minpet/>

theriak/theruser.html). Modeling was conducted in the 11-component system $\text{MnO-Na}_2\text{O-CaO-K}_2\text{O-FeO-MgO-Al}_2\text{O}_3\text{-SiO}_2\text{-H}_2\text{O-TiO}_2\text{-Fe}_2\text{O}_3$ (MnNCKFMASHTO) using the internally consistent thermodynamic dataset tc-db55 of Holland & Powell (1998; updated August, 2004). Whole-rock composition (Supplementary Data Electronic Appendix 1, Table A8.1) was determined by ICP-MS (Activation Laboratories Ltd., Canada). The method used to construct the phase diagram models is described in Supplementary Data Electronic Appendix 1.

Garnet compositional isopleths of grossular and pyrope were contoured on each phase diagram in an attempt to track a portion of the P - T history as recorded by the garnet end-member compositions. As discussed above, diffusive homogenization of prograde growth zoning at peak conditions, followed by retrograde reactions (Fig. 8), precludes the use of core-to-rim garnet compositions for interpreting the P - T conditions coincident with garnet growth. Instead, the composition with the highest pyrope value is considered the best estimate of the composition of syn- D_1 garnet at the thermal peak (arrows in Fig. 8; e.g. Weller *et al.*, 2013). The garnet compositions used to estimate peak P - T are presented in Supplementary Data Electronic Appendix 2. The thermal peak conditions are also constrained using peak assemblages interpreted from petrography. The vol. % values of solid phases at the estimated peak conditions were calculated using Theriak and compared with modal abundances estimated in thin section (Supplementary Data Electronic Appendix 1, Table A10.1). The Ti-in-biotite geothermometer (Henry *et al.*, 2005) is calibrated for graphitic, ilmenite- or rutile-bearing, peraluminous pelites that equilibrated at *c.* 4–6 kbar, and was applied to sample S145A as it is the only sample that meets the calibration criteria. The Ti-in-biotite geothermometer was applied to five matrix biotite grains, including some in contact with garnet.

For any P - T point on the model phase diagrams, the 1σ uncertainty is suggested to be ± 0.5 kbar and $\pm 25^\circ\text{C}$ (Powell & Holland, 2008). These are minimum error estimates, particularly given the uncertainty involved in estimating the composition of garnet at the thermal peak. Although the maximum pyrope compositions coincide with enriched X_{Grs} cores that may reflect prograde conditions, variations in X_{Grs} from core to rim in three samples (~ 0.005 cation mole fraction) are beyond the resolution of phase diagram models and have negligible effects on our P - T estimates. The more pronounced grossular zoning in sample F122B only slightly affects our estimated peak conditions (see below).

Phase diagram models

Sample F122B: mid-amphibolite-facies pelite

The composition of syn- D_1 garnet at the thermal peak, estimated at the highest pyrope value, corresponds to intersecting grossular (0.05) and pyrope (0.14) isopleths at ~ 6.25 kbar and $\sim 740^\circ\text{C}$, constraining the thermal

peak above the onset of muscovite dehydration melting (point P, Fig. 9). The modeled thermal peak plots in a stability field defined by the peak assemblage interpreted from petrography (dark grey shaded field, Fig. 9a). Additionally, petrographical evidence of ~ 15 vol. % leucosome containing $\text{Pl} + \text{Qz} \pm \text{Kfs}$, interpreted as former melt (Fig. 5d), substantiates the estimated thermal peak above temperatures required to initiate melting. Elevated grossular (~ 0.06) in garnet cores suggests a clockwise, prograde path at higher pressures (~ 7 – 8 kbar), although Ca in garnet may have been modified during peak conditions. Lower grossular in garnet rims (~ 0.04) implies lower pressures (~ 5.1 kbar) at the thermal peak, although within the same stability field. The abundance of post- D_1 muscovite in sample F122B (Fig. 5c–f), along with the rarity of K-feldspar, suggests subsequent cooling below the solidus and the retrograde reversal of muscovite breakdown reactions. Partially resorbed garnet rims and late adjacent biotite growth (Fig. 5c) may also be consistent with a retrograde overprint. The vol. % of phases modeled using Theriak (Supplementary Data Electronic Appendix 1, Table A10.1) at the estimated peak conditions (740°C , 6.25 kbar) is in agreement with the vol. % estimated from petrography when retrograde growth of muscovite at the expense of K-feldspar is accounted for.

Sample S89A: mid-amphibolite-facies pelite

The highest Mg garnet composition coincides with grossular (0.04) and pyrope (0.14) isopleths at ~ 7.25 kbar and 715°C (point P, Fig. 10). These P - T conditions are within a narrow, K-feldspar-absent stability field containing $\text{Grt-Ms-Bt-Sil-Qz-Liq}$, at sufficient temperatures to allow K-feldspar-absent muscovite breakdown. However, within 1σ uncertainty (± 0.5 kbar and 25°C ; Powell & Holland, 2008), the modeled thermal peak could be up to $\sim 740^\circ\text{C}$, hot enough to allow muscovite dehydration melting and produce the peak assemblage interpreted from petrography (grey shaded field, Fig. 10a). Partial melting is substantiated by lenses of coarse-grained leucogranite in outcrop, as well as ~ 5 vol. % leucosome in hand sample. Muscovite breakdown is also in accordance with the presence of sillimanite inclusions in garnet and fine-grained sillimanite aggregates, as well as coarse-grained sillimanite in outcrop. In particular, textures suggest that post- D_1 muscovite formed from rehydration of K-feldspar, a product of muscovite dehydration melting. Subsequent cooling across the solidus into a muscovite-bearing, sillimanite-absent stability field is inferred from the replacement of K-feldspar by late muscovite, as well as S_1 -parallel bands of fine-grained muscovite that are interpreted to represent retrograde pseudomorphs of faserkiesel (fibrolite + $\text{Qz} \pm \text{Kfs}$; Fig. 5g and h). Furthermore, the vol. % values of phases (modeled in Theriak) at 715°C and 7.25 kbar do not correspond to those of phases in thin section; in particular, Theriak calculates <1 vol. % sillimanite at these conditions. The modeled vol. %

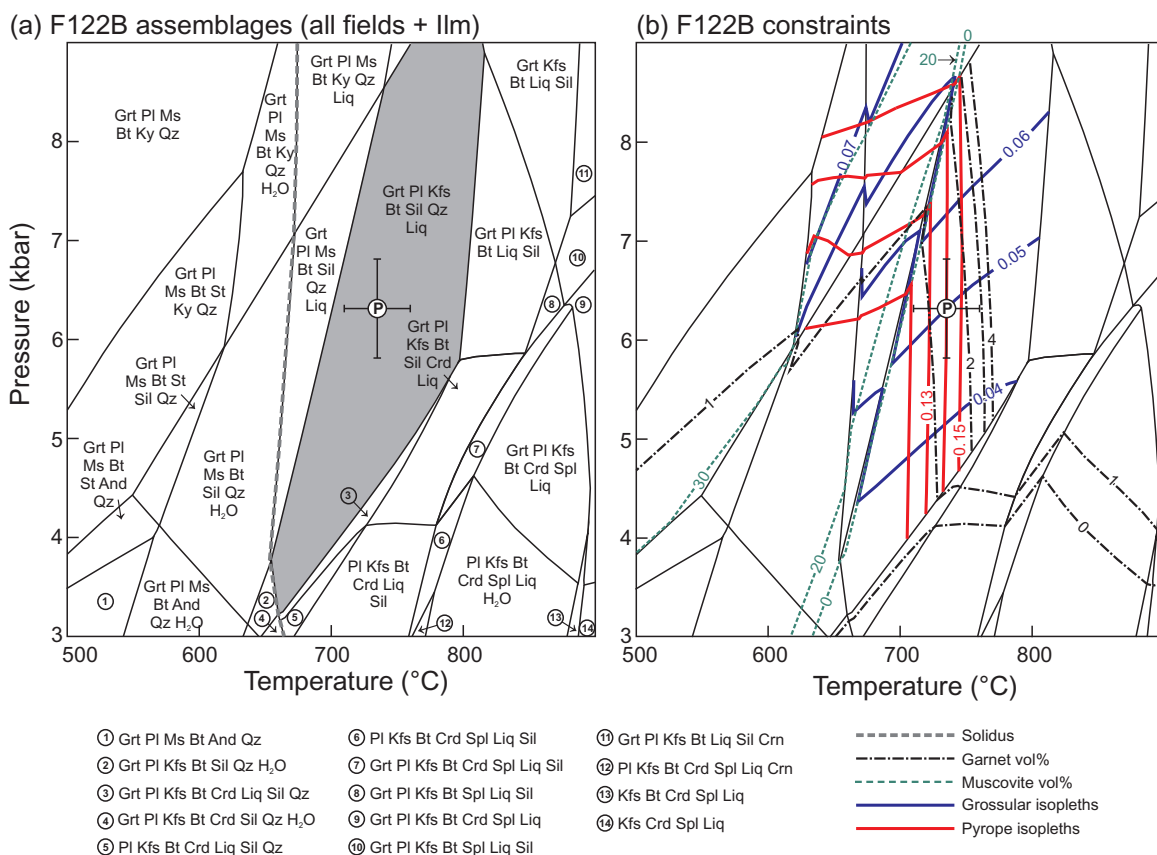


Fig. 9. Equilibrium phase diagram model for sample F122B (see [Supplementary Data Electronic Appendix 1, Table A8.1](#) for bulk composition). Point P corresponds to modeled thermal peak conditions ($\pm 1\sigma$) based on the estimated composition of garnet at the thermal peak (arrow in [Fig. 8](#)) and corresponding pyrope and grossular isopleths. (a) F122B model with all assemblage fields labelled. The peak assemblage field is shaded grey. (b) F122B model with isopleths for pyrope and grossular in garnet and for vol. % garnet and muscovite.

values of phases for temperatures of 730–740°C and 7.25 kbar include ~11% sillimanite and align more closely with modal abundances observed in thin section when retrograde replacement of K-feldspar by muscovite is accounted for.

Sample F28A: upper-amphibolite-facies psammite

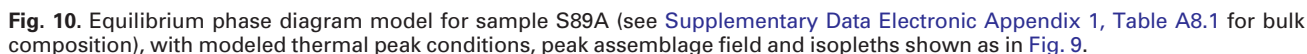
In the modeled phase diagram for sample F28A, the grossular (0.034) and pyrope (0.30) contents of the peak garnet composition correspond to conditions of ~7.1 kbar and 810°C in a stability field containing Grt–Kfs–Bt–Liq–Sil–Qz (point P in [Supplementary Data Electronic Appendix 1, Fig. A11.1](#)). The modeled thermal peak is at sufficiently high temperatures to allow muscovite dehydration melting, as interpreted from petrography. However, sample F28A contains approximately equal amounts of K-feldspar and plagioclase. On the phase diagram, the peak assemblage interpreted from petrography (Grt–Pl–Kfs–Bt–Liq–Sil–Qz; grey shaded field in [Supplementary Data Electronic Appendix 1, Fig. A10.1](#)) has a higher P – T range (7–9 kbar and ~810–850°C) than the thermal peak estimated from the peak garnet composition. The discrepancy between the modeled thermal peak and the observed peak assemblage may be due to intra-grain diffusion in garnet. If the pyrope

content of garnet during the thermal peak was higher than the estimated 0.30 (point P), the garnet composition may correspond to intersecting isopleths in the modeled peak assemblage field. In addition, the discrepancy may be attributed to the effect of melt loss on the modeled bulk composition. If significant melt loss occurred, a phase diagram constructed using the measured bulk-rock composition allows investigation of only the post-melt-loss history (e.g. [Indares *et al.*, 2008](#); [Guilmette *et al.*, 2011](#)).

Considerations of melt loss

Melt loss is not considered to have significantly affected the model phase diagrams for samples F122B and S89A because of the lack of connected melt channel networks and low leucosome volume (~5–10%) in outcrop, and the presence of ~5–15 vol. % leucosome in the analyzed bulk-rock samples. Furthermore, the modeled phase diagrams predict the observed peak assemblages and vol. % of phases at reasonable P – T ranges that correspond to peak garnet compositions.

Petrographic evidence suggests that muscovite in sample F28A was consumed by vapour-absent muscovite dehydration melting, and that some biotite dehydration melting may have occurred; however, the



garnet compositional isopleths in an attempt to infer the peak P - T . This method assumes that melt loss occurred after the compositional equilibration of garnet, which is plausible as most melt loss typically occurs during decompression after the thermal peak (e.g. Brown, 1994, 2004).

The melt-integrated phase diagram model of sample F28A more accurately reflects the observed mineral phases, including both K-feldspar and plagioclase, but has a large built-in degree of uncertainty owing to the assumptions used in melt integration. The peak composition of garnet corresponds to intersecting isopleths at ~ 7.2 kbar and 810°C (point P, Fig. 11), in a Grt-Pl-Kfs-Bt-Liq-Sil-Q stability field. The melt-integrated phase diagram model predicts peak conditions sufficient for vapour-absent muscovite dehydration melting, consistent with petrographic observations of coarse-grained leucosomes, abundant K-feldspar and sillimanite, and the absence of muscovite. The modeled thermal peak conditions are also consistent with orthopyroxene- and cordierite-absent biotite dehydration melting, a continuous reaction that occurs above $\sim 750^{\circ}\text{C}$ (Spear & Parrish, 1996; Spear *et al.*, 1999). At the estimated peak conditions (point P), the vol. % values of phases modeled by Theriak generally agree with the modal

abundances observed in thin section, although Theriak suggests less biotite at the thermal peak (6%) than that actually observed (~15 vol. %). Some retrograde biotite may have formed during melt crystallization. Given the significant inherent assumptions with the melt-integrated model (as discussed above), we consider ~7.2 kbar and 810°C (point P, Fig. 11) as a reasonable, but semi-quantitative, thermal peak P – T estimate for sample F28A.

Sample S145A: granulite-facies pelite

On the model phase diagram, the interpreted peak mineral assemblage for sample S145A (Grt–Crd–Kfs–Sil–Pl–Qz–Ilm–Liq) spans ~810–890°C and 6.1–7.35 kbar (dark grey shaded field, Fig. 12a). The modeled peak P – T conditions are consistent with field and petrographic evidence of biotite dehydration melting at granulite-facies conditions. However, the grossular and pyrope isopleths do not intersect over the compositional range of garnet (Fig. 12b), and the estimated 'peak' garnet composition (pyrope = 0.33; grossular = 0.03) cannot be plotted. Because >40 vol. % melt can be generated after biotite dehydration melting (Patiño-Douce & Johnston, 1991), sample S145A probably underwent significant melt loss. This is supported by the restitic nature of S145A, which is dominated by garnet, cordierite and sillimanite, with only ~10 vol. % *in situ* former melt in the hand sample, whereas a stromatic, interconnected melt network occurs in outcrop (Supplementary Data Electronic Appendix 1, Fig. A2.1e and f). Melt integration modeling was not attempted given the large volumes of melt that would need to be considered. The phase diagram model for sample S145A is considered to be non-quantitative, but it yields helpful information about peak and post-peak metamorphism. The vol. % abundances of phases modeled by Theriak over the P – T range of ~850–890°C and 7–7.35 kbar are close to those of phases estimated in thin section when retrograde biotite growth is accounted for.

Using the Ti-in-biotite geothermometer (Henry *et al.*, 2005), five matrix biotite grains yielded consistent temperature estimates of 771–794°C, including biotite in contact with garnet and grains surrounded by feldspar and quartz. The average temperature of $782 \pm 12^\circ\text{C}$ corresponds to fields where biotite is stable (e.g. light grey shaded field, Fig. 12a), suggesting that sample S145A underwent a reversal of biotite dehydration melting reactions during cooling. Cooling to a biotite-bearing stability field is supported by observations of ~5% biotite in thin section, often concentrated along embayed garnet rims (Fig. 6c), in addition to high Fe/(Fe + Mg) in garnet rims. The consumption of garnet rims by cordierite (Fig. 6d) may have occurred during cooling, possibly by the reaction $\text{Grt} + \text{Kfs} + \text{Liq} = \text{Crd} + \text{Bt}$ (Spear *et al.*, 1999), or during decompression post-thermal peak, potentially by the reaction $\text{Grt} + \text{Sil} + \text{Qz} = \text{Crd}$ (Bhattacharya, 1993). Cooling and decompression are

illustrated by the possible retrograde P – T path depicted in Fig. 12.

MONAZITE GEOCHRONOLOGY

Analytical methods

Monazite was dated *in situ* in four metasedimentary rocks to resolve the timing of metamorphism and fabric development. In each sample, 15–30 monazite grains were dated using LA-ICP-MS at the University of New Brunswick (Canada) following the analytical methods in Supplementary Data Electronic Appendix 1. Monazite grains were dated in several microstructural contexts, including along grain boundaries as well as inclusions in matrix minerals and in garnet, and monazite aligned with S_1 . Grains of sufficient size were analyzed using 2–4 analytical spots with a 10–13 µm spot diameter to date prospective age domains. The corresponding U–Pb analytical data are provided in Supplementary Data Electronic Appendix 3. For each sample, all analyses were initially plotted on a concordia diagram using Isoplot v4 (Ludwig, 2003) but no single age could be resolved owing to the single spot age scatter. For each sample, statistical evaluations of concordia diagrams and weighted average plots of $^{206}\text{Pb}/^{238}\text{U}$, $^{207}\text{Pb}/^{235}\text{U}$ and $^{207}\text{Pb}/^{206}\text{Pb}$ ages were used to identify groups of three or more analyses that cluster on concordia and yield a statistically valid concordia age with a combined MSWD (of concordance and X – Y equivalence) of less than two. The concordia age is reported for each sample in this study, at 2σ uncertainty, representing the weighted mean age of n number of analyses on a concordia diagram (Ludwig, 2003). Discordant monazite analyses were not included in the analysis clusters that were used to calculate ages. In samples F122B, S89A and S145A, two or three monazite grains with multiple age domains were selected for trace element mapping using LA-ICP-MS (University of New Brunswick, Canada). Analytical methods and compositional maps are presented in Supplementary Data Electronic Appendix 1 (Fig. A13.1–3).

In situ U–Pb geochronology results

Sample F122B: mid-amphibolite-facies pelite

In sample F122B, monazite typically forms subhedral, 40–100 µm long grains that are concentrated in syn- S_1 biotite. No monazite was found in garnet, plagioclase, quartz or leucosomes. Twenty-one analyses of 15 monazite grains form a concordant cluster at 1831 ± 5 Ma (MSWD = 0.72; Fig. 13a). Most monazite grains are S_1 -aligned and five grains have multiple analyses that plot in the c. 1831 Ma age cluster, with no other apparent age domains (Fig. 14a and b). The cluster also includes an analysis from a grain that contains several <10 µm long aluminosilicate inclusions aligned parallel to S_1 , as well as a grain that has two additional discordant analyses at c. 1900 Ma. Some grains exhibit patchy, irregular zoning in back-scattered electron

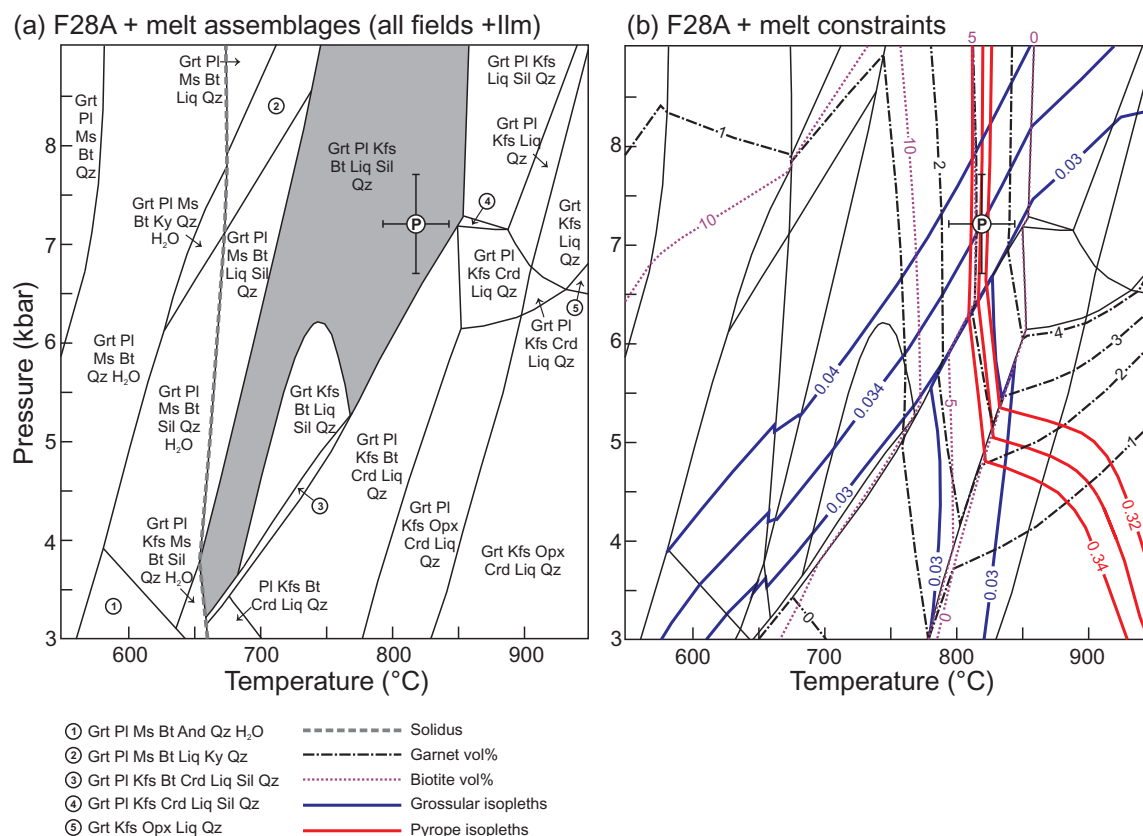


Fig. 11. Equilibrium phase diagram model for sample F28A with 10% melt integrated into the bulk composition (see [Supplementary Data Electronic Appendix 1, Table A8.1](#) for bulk composition). Details of melt integration method are given in text. Point P corresponds to modeled thermal peak conditions ($\pm 1\sigma$) based on the estimated composition of garnet at the thermal peak (arrow in [Fig. 8](#)) and corresponding pyrope and grossular isopleths. (a) Model using bulk composition of F28A + melt, with all assemblage fields labelled and the peak assemblage field shaded grey. (b) F28A model with isopleths for pyrope and grossular in garnet and for vol. % garnet and biotite.

(BSE) images, but there is no clear relationship between dark- or light-BSE domains and age.

Sample S89A: mid-amphibolite-facies pelite

In sample S89A, monazite forms 20–50 μm , subhedral, subequant grains, and less commonly elongate, S_1 -aligned grains up to 200 μm long. Seventeen analyses from 12 grains yield an age of 1808 ± 4 Ma (MSWD = 1.2; [Fig. 13b](#)), which includes analyses from S_1 -aligned matrix monazite ([Fig. 14c](#)), as well as one analysis from an inclusion in a garnet rim ([Fig. 14d](#) and [e](#)). Some grains have multiple analyses that are all included in the c. 1808 Ma cluster (or are younger and discordant), with no other apparent age domains. These comprise subequant grains in biotite or along grain boundaries, as well as subhedral-to-anhedral, elongate monazite grains that appear intergrown with fine-grained muscovite that is interpreted as post- D_1 , retrograde muscovite ([Fig. 14f](#)). Six analyses from six grains form an additional concordant cluster at 1852 ± 7 Ma (MSWD = 1.5), including analyses from subequant monazite grains in the matrix, from monazite aligned with S_1 in biotite ([Fig. 14c](#)) and one analysis from a monazite inclusion in a garnet rim ([Fig. 14d](#) and

[e](#)). Most analyses in the c. 1852 Ma cluster are from grains with additional analyses that are included in the c. 1808 Ma group ([Fig. 14c–e](#)) or are younger and discordant. Zoning in BSE is rare, but the older and younger age domains generally correspond to grain interiors and edges, respectively.

Sample F28A: upper-amphibolite-facies psammite

In sample F28A, monazite forms 20–60 μm grains that are mostly subhedral and equant, and are concentrated in garnet- and biotite-rich bands. Monazite grains occur in matrix biotite, quartz and feldspar, along grain boundaries and also define S_1 -aligned inclusion trails in garnet ([Fig. 14g](#)). Ten analyses from five grains form a cluster on a concordia plot that yields an age of 1825 ± 8 Ma (MSWD = 0.74; [Fig. 13c](#)); this includes two analyses from an elongate monazite in an S_1 -parallel inclusion trail in garnet ([Fig. 14g](#)). Four additional c. 1880–2000 Ma dates are from single analysis monazite grains in the matrix and inclusion trails in garnet.

Sample S145A: granulite-facies pelite

Monazite in sample S145A forms 30–100 μm , subhedral, equant grains. Thirty-five analyses from 22 grains yield

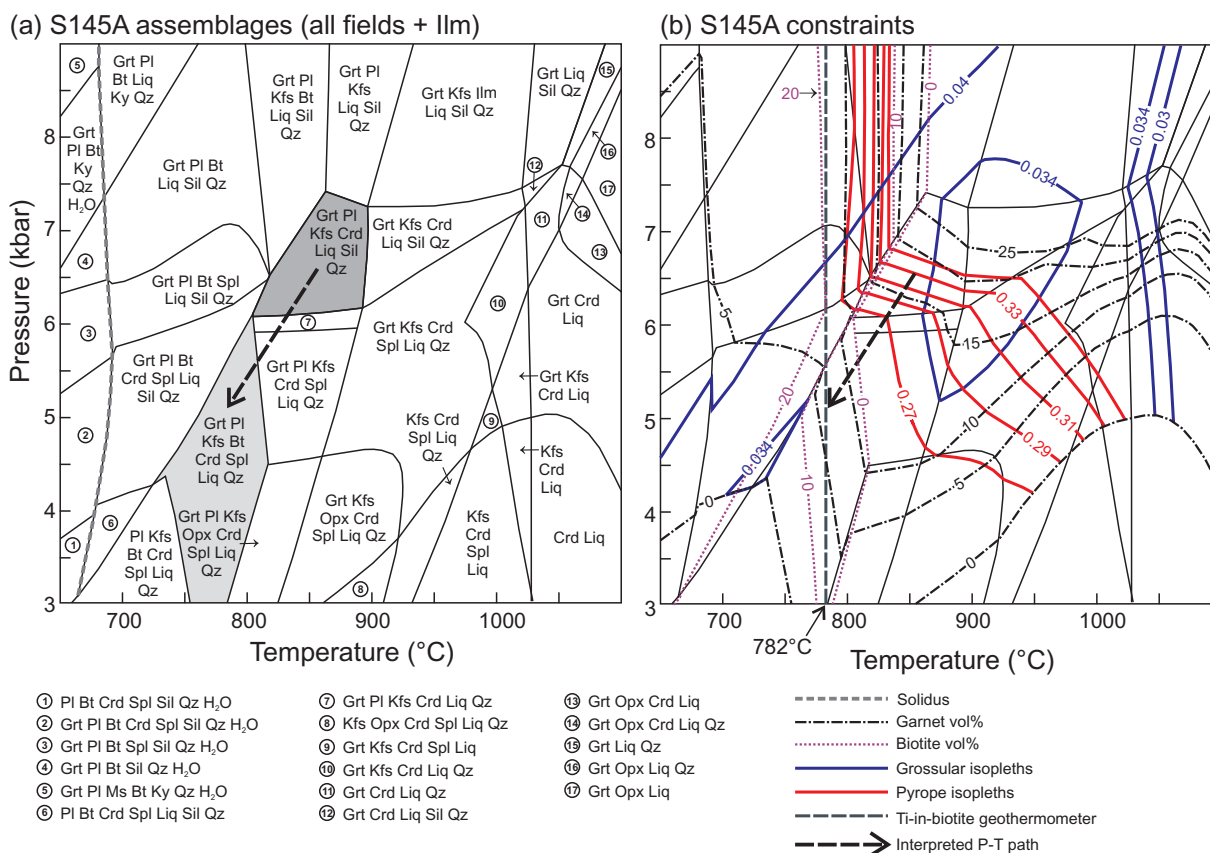


Fig. 12. (a) Equilibrium phase diagram model for sample S145A (see [Supplementary Data Electronic Appendix 1, Table A8.1](#) for bulk composition), with all assemblage fields labelled and with an interpreted decompressive cooling path (dashed arrow) from the stability field of the peak assemblage (shaded dark grey) to a stability field with stable biotite (shaded light grey). (b) S145A model with isopleths for pyrope and grossular in garnet and for vol. % garnet and biotite, showing the temperature calculated from the Ti-in-biotite geothermometer.

an age of 1830 ± 4 Ma (MSWD = 1.5; [Fig. 13d](#)), including analyses from monazite in S_1 -parallel matrix minerals (plagioclase, K-feldspar, cordierite, quartz; [Fig. 14h](#)). Several c. 1830 Ma monazite grains occur in S_1 -aligned inclusion trails in garnet, along with sillimanite and biotite ([Fig. 14i](#) and [j](#)). A second concordant cluster is formed by nine analyses from eight matrix monazite grains at 1799 ± 6 Ma (MSWD = 0.86). Several grains have two or more analyses with different ages that typically correspond to grain interiors or edges and/or BSE zoning. For example, eight grains have c. 1830 Ma cores and are typified by dark BSE contrast, surrounded by c. 1799 Ma rims that are light in BSE ([Fig. 14k](#)). Three grains contain domains of variable BSE shades that are c. 1850 Ma or older, surrounded by c. 1830 Ma rims. In other grains, multiple analyses all plot within the c. 1830 Ma age cluster, despite apparent zonation in BSE.

Monazite trace element mapping results

In granulite-facies sample S145A and mid-amphibolite-facies sample S89A, c. 1800 Ma domains are depleted in Y, Yb, Eu (\pm Gd) relative to c. 1850–1830 Ma cores ([Supplementary Data Electronic Appendix 1, Figs A13.2 and A13.3](#)). In mid-amphibolite-facies sample F122B, c.

1800 Ma monazite domains are generally Y- and Yb-enriched relative to c. 1850–1830 Ma cores ([Supplementary Data Electronic Appendix 1, Fig. A13.1](#)). Compositional zoning patterns of monazite in each sample range from concentric core-to-rim zonation to complex, patchy patterns.

DISCUSSION

Interpretation of metamorphism and mineral fabric relationships

The mineral fabric relationships, mineral compositions and modeled P - T estimates strongly support the field-based interpretation of a metamorphic field gradient ([Fig. 3](#)) characterized by a westward increase in peak metamorphic grade from mid-amphibolite facies (~ 720 – 740°C) to granulite facies (~ 850 – 890°C) at medium pressures (~ 6 – 7 kbar). Because D_1 fabrics are defined by peak metamorphic minerals and leucosomes are also parallel to S_1 ([Figs 5–7](#); [Supplementary Data Electronic Appendix 1, Figs A2.1 and A2.2](#)), peak metamorphism and partial melting are interpreted as concurrent with D_1 east-vergent crustal shortening.

Post- D_1 retrograde micas occur in each metamorphic zone, including post- D_1 biotite that occupies embayments in garnet rims. Post- D_1 muscovite in the eastern mid-amphibolite-facies zone is considered to represent the retrograde reversal of muscovite breakdown reactions following cooling below the solidus after the syn- D_1 thermal peak. Because most post- D_1 retrograde muscovite grains in sample F122B are axial planar to F_3 crenulations, but some cross-cut F_3 crenulations, post- D_1 retrograde muscovite growth probably continued as late as post- D_3 (Fig. 7).

Although the pre- and post-thermal-peak P - T history is not constrained quantitatively, grossular-rich garnet cores and decompression textures in some samples may be reflections of clockwise P - T paths. This might suggest that Hall Peninsula followed an overall clockwise P - T evolution with peak metamorphism ranging from mid-amphibolite to granulite facies, followed by cooling and decompression (Fig. 15).

Interpretation of geochronology

Significant monazite growth can occur during amphibolite- to granulite-facies metamorphism pre-thermal peak, at thermal peak, during melt crystallization and during retrograde garnet consumption (Pyle & Spear, 2003; Mahan *et al.*, 2006; Spear & Pyle, 2010). Together, the *in situ* U-Pb monazite and petrological data suggest that the dominant c. 1831–1825 Ma monazite population records the timing of regional amphibolite- to granulite-facies metamorphism, concurrent with east-directed D_1 shortening. This is conclusively demonstrated by the abundance of S_1 -aligned c. 1831–1825 Ma monazite in the matrices of all samples, as well as c. 1831–1825 Ma monazite that occurs with prograde to peak mineral assemblages in S_1 -aligned inclusion trails in garnet (Fig. 14). In each sample, analysis clusters that yield ages of c. 1831–1825 Ma include analyses that are c. 1850–1840 Ma in age (Figs 13 and 14a–e, g–k). The subordinate population of c. 1852 Ma monazite in sample S89A possibly records prograde to peak metamorphism as it includes analyses from S_1 -aligned matrix grains (Fig. 14c) and an inclusion in garnet (Fig. 14d and e). Therefore, the data imply that regional high-grade metamorphism and concomitant D_1 deformation span c. 1850 to 1825 Ma.

Petrographic relationships of c. 1800 Ma age domains suggest that monazite formation at c. 1800 Ma postdates peak metamorphism by at least 25 Myr. Samples with c. 1800 Ma monazite also contain c. 1850–1825 Ma monazite, with the younger population commonly forming domains adjacent to c. 1850–1825 Ma domains (Fig. 14b–e and i–k), which are interpreted as coincident with thermal peak conditions. The c. 1800 Ma monazite domains appear to postdate garnet growth and D_1 because they are mostly in the matrix but do not clearly define a structural fabric. Rare occurrences of c. 1800 Ma monazite included in

garnet are typically close to microfractures in garnet rims (Fig. 14d).

Monazite trace element maps indicate that the Y, Yb and Eu (\pm Gd) compositions of c. 1800 Ma domains are distinct from c. 1850–1825 Ma interiors. Evidence of garnet resorption in sample F122B supports garnet breakdown as a possible source for the Y-rich c. 1800 Ma domains (e.g. Pyle & Spear, 1999; Foster *et al.*, 2002), but Y-depleted c. 1800 Ma domains in other samples suggest that variable trace element compositions in c. 1800 Ma monazite resulted from a more complex process. The petrological data indicate post- D_1 retrograde muscovite growth, retrograde reversal of biotite dehydration reactions and Fe–Mg exchange between garnet and biotite. Limited petrographic evidence (sample S89A) suggests that post-thermal-peak monazite formation was coeval with retrograde muscovite growth (Fig. 14f). Because fluids are essential for retrograde mineral growth (Vernon & Ransom, 1971), monazite may have undergone fluid-assisted coupled dissolution–reprecipitation (Seydoux-Guillaume *et al.*, 2002; Harlov & Hetherington, 2010; Williams *et al.*, 2011). The complex BSE zoning patterns exhibited by many monazite grains with within-grain age variation (e.g. Fig. 14b, c, e, j and k) are similar to those formed by fluid-assisted dissolution–reprecipitation in natural and experimentally altered monazite (Harlov & Hetherington, 2010; Williams *et al.*, 2011). The trace element maps of monazite with c. 1800 Ma and older domains reveal concentric core-to-rim compositional zoning in some grains and patchy, irregular zoning in others, which may also be consistent with coupled dissolution–reprecipitation. Considering the catalyzing effect of strain on dissolution–reprecipitation (Wawrzenitz *et al.*, 2012), monazite formation at c. 1800 Ma may have been triggered by post-thermal-peak deformation.

Given the range of monazite ages identified in our four samples, the monazite geochronology presented here provides preliminary age constraints on the P - T - d evolution, which would be improved by additional comprehensive *in situ* monazite analyses on regionally distributed samples. Nonetheless, when combined with previously published geochronology, the data allow preliminary interpretations of the regional tectonothermal history (see below).

Tectonic implications

Regional metamorphism and crustal shortening (D_1 and D_2)

Based on the integrated petrological–geochronological data presented above, the study area underwent east-directed crustal shortening (D_1) and regional metamorphism at c. 1850–1825 Ma (Fig. 15). The minimum age of D_1 is provided by the 1830 ± 3 Ma age of a monzogranite dike that cross-cuts S_1 in metasedimentary host rocks (Rayner, 2015). Thick-skinned, east-vergent D_2 thrusts and folds are interpreted as syn- to post-

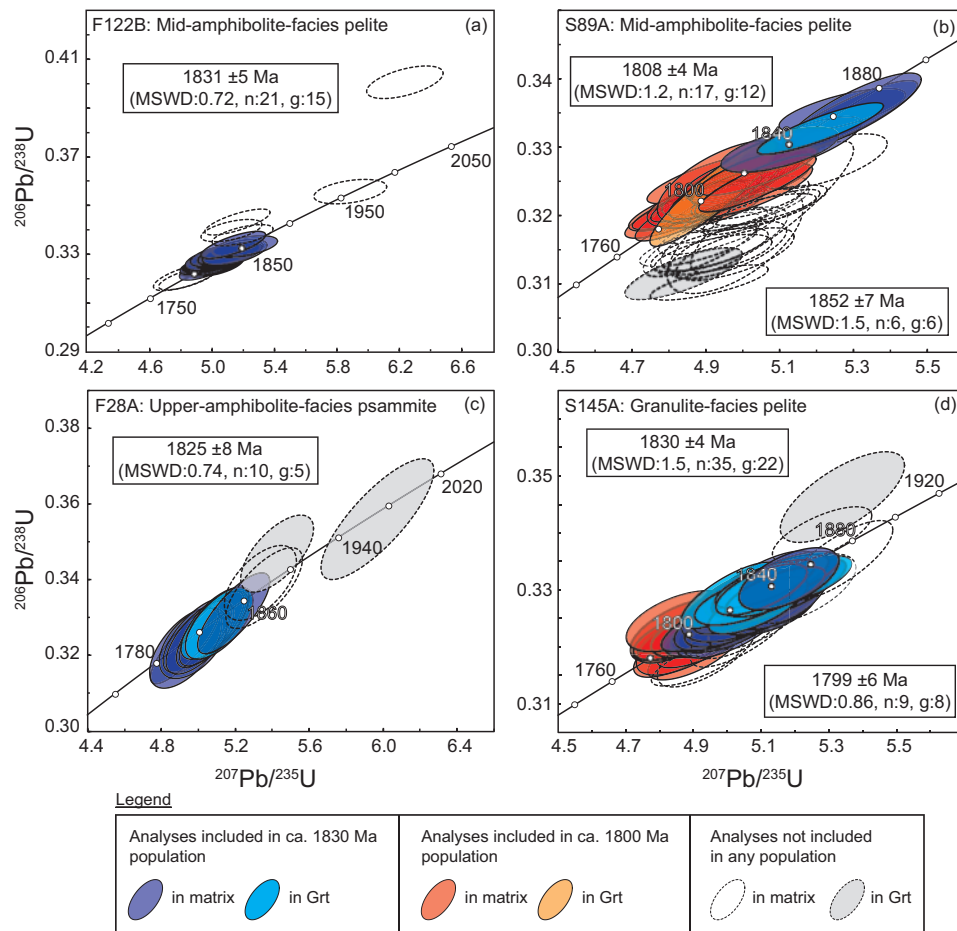


Fig. 13. Concordia plots of *in situ* U–Pb monazite analyses in samples (a) F122B, (b) S89A, (c) F28A and (d) S145A, showing calculated concordia ages ($\pm 2\sigma$ Ma). In sample F28A, one concordant ellipse at ~ 3000 Ma is not shown.

thermal peak, and are therefore estimated to have occurred during or after *c.* 1850–1825 Ma.

High-grade metamorphism in the study area at *c.* 1850–1825 Ma is coeval with granulite-facies metamorphism and deformation on the southern MIM, which has been attributed to the collision of the Narsajuaq terrane and emplacement of the Cumberland Batholith (St-Onge *et al.*, 2007) or the impingement of the Archean crystalline Sugluk Block beneath the MIM (Corrigan *et al.*, 2009; Whalen *et al.*, 2010). These events on the MIM are coeval with north–south accretion of the composite Rae craton and Asiaat domain with the North Atlantic craton in West Greenland, and with the collision of the North Atlantic craton with the MIM in Labrador and Quebec (St-Onge *et al.*, 2009, and references therein). This strengthens the proposed correlations between the eastern MIM and the Asiaat domain of West Greenland (e.g. St-Onge *et al.*, 2009), and with the Core Zone in north-central Labrador (e.g. Corrigan *et al.*, 2009; St-Onge *et al.*, 2009).

Heat flow from concurrent orthopyroxene-bearing intrusions (Cumberland Batholith) may have contributed to *c.* 1850–1825 Ma granulite-facies metamorphism in the study area. However, elevated radioactive heat production in thickened crust (e.g. England & Thompson,

1984; Jamieson *et al.*, 1998; Brown, 2006; Clark *et al.*, 2011), or increased heat flow in a former back-arc basin setting (e.g. Brown, 2006; Clark *et al.*, 2011) may have played significant roles. The Cumberland Batholith represents continental, Andean-type arc magmas that were emplaced into the accreted MIM and Rae craton margin (Hoffman, 1990; Thériault *et al.*, 2001; St-Onge *et al.*, 2006, 2007), or were largely derived from post-accretion lithospheric mantle delamination and melting of the subducted Sugluk Block from beneath the MIM (Whalen *et al.*, 2010). In either scenario, the study area on the eastern MIM would probably have been in a back-arc setting, which is in accordance with the following: (1) attainment of granulite-facies conditions; (2) derivation of mafic sills in supracrustal sequences from partial melting of a subduction-modified mantle (MacKay & Ansdell, 2014); (3) NE-dipping teleseismic discontinuities in the upper mantle beneath the southern MIM that may represent the underthrust Narsajuaq arc and Sugluk Block (Snyder, 2010); (4) mantle xenoliths in kimberlite containing garnet with oceanic and continental sources, which imply that subducted material extends northeastwards beneath the study area (Snyder, 2010). Peak metamorphism and crustal shortening at *c.* 1850–1825 Ma could plausibly reflect subduction (of Narsajuaq arc or Sugluk

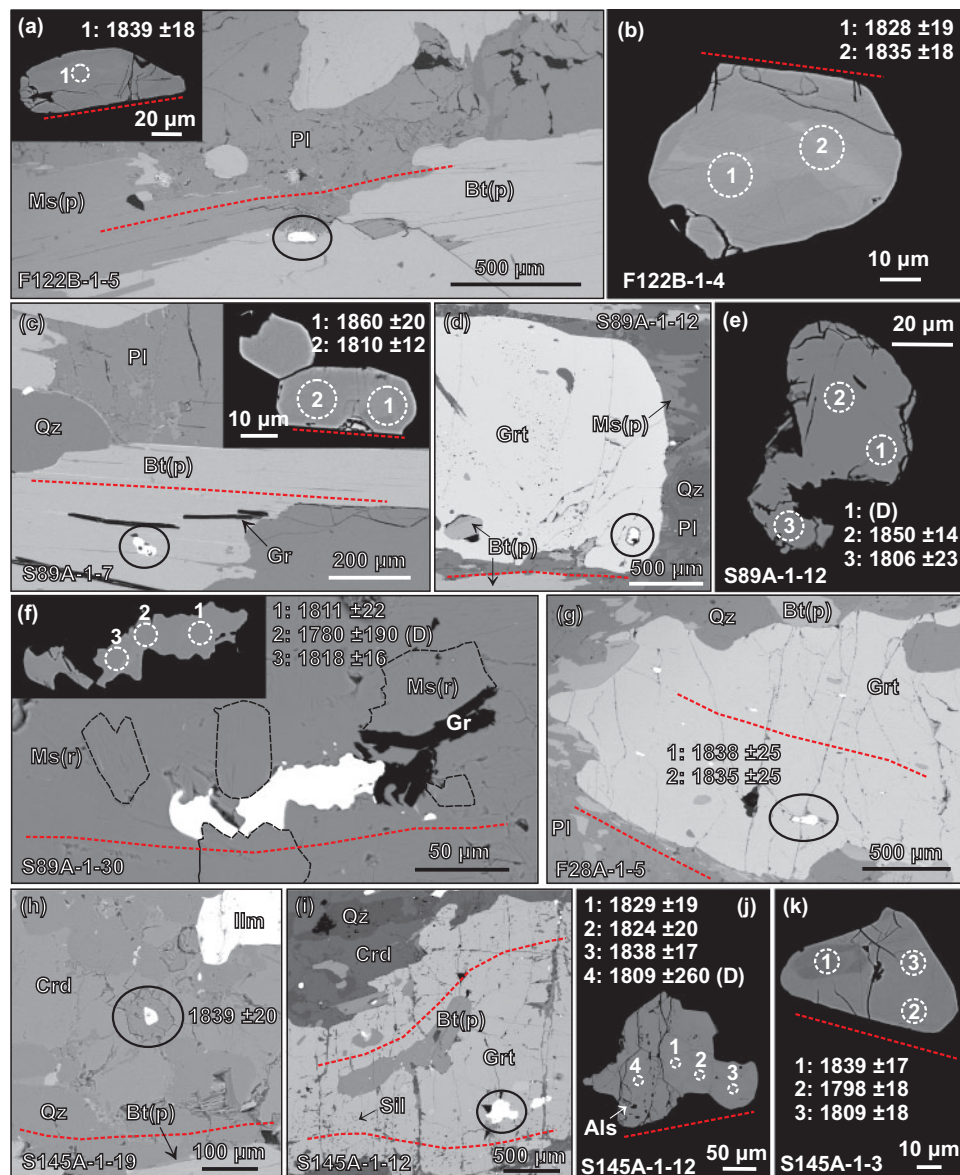


Fig. 14. Representative SEM back-scattered electron (BSE) images of monazite dated from Hall Peninsula. In sample numbers, the number after first hyphen is thin section number and that after second hyphen is grain number (e.g. F122B-1-5). Red dashed lines indicate S_1 fabric orientation. Laser pit locations are circled in white and labelled with analysis number and concordia age ($\pm 2\sigma$) in Ma; (D) denotes discordant analyses. (a, b) Examples of c. 1830 Ma monazite aligned with S_1 in the matrix of F122B. (c–e) Examples of monazite in S89A with c. 1850 Ma and c. 1800 Ma domains aligned with S_1 in the matrix (c) and in Grt (d, e). (f) A monazite grain that appears intergrown with post- D_1 retrograde Ms in S89A. (g) A c. 1830 Ma monazite grain in an S_1 -aligned inclusion trail in Grt in F28A. (h–k) Examples of c. 1830 Ma monazite in S145A in S_1 -aligned Crd (h), in an S_1 -aligned inclusion trail in Grt (i, j) and containing c. 1800 Ma domains (j, k).

block?) beneath the MIM and the progressive closure of a back-arc basin on Hall Peninsula. The eastward decrease in metamorphic grade may be attributed to a greater inboard distance from the Andean-style margin, resulting in lower heat flow as well as thinner, more distal supracrustal cover sequences and less crustal thickening.

Late-orogenic activity

As discussed above, monazite formation at c. 1800 Ma is probably the result of fluid-assisted dissolution–

reprecipitation that occurred at least 25 Myr after the thermal peak, possibly activated by a late-orogenic deformation event. Significantly, regional monazite formation at c. 1800 Ma is coeval with the 1820–1795 Ma docking of the Superior craton with the Churchill plate, considered to represent the terminal collision of the THO (St-Onge *et al.*, 2007, 2009; Corrigan *et al.*, 2009, and references therein). This resulted in amphibolite-facies metamorphism at c. 1820–1810 Ma and the development of localized shear zones on the MIM (St-Onge *et al.*, 2007). Potentially, c. 1800 Ma monazite in the study area may be related to the THO terminal collision;

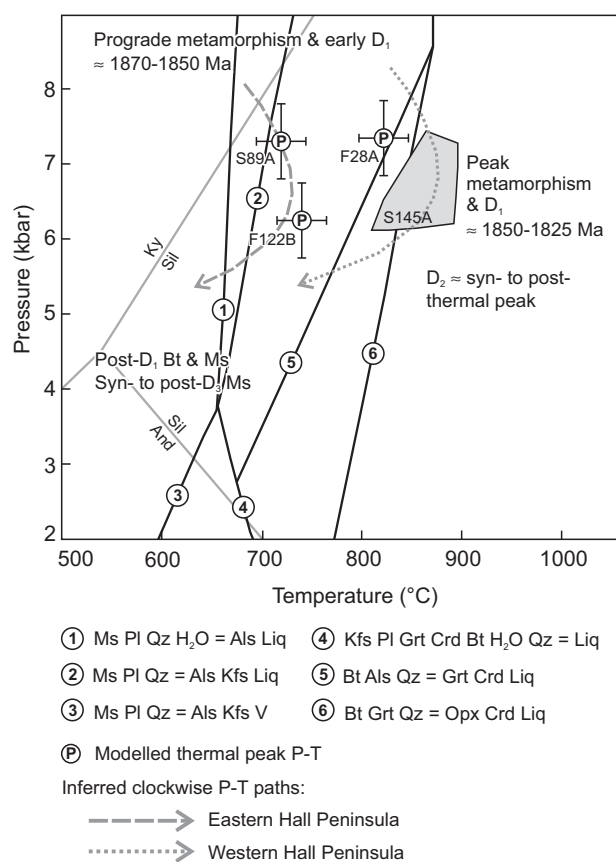


Fig. 15. Summary of the pressure–temperature–deformation evolution of the metamorphic rocks on Hall Peninsula interpreted from the modeled thermal peak P – T conditions and *in situ* U–Pb monazite ages in this study. Clockwise P – T paths are inferred from grossular-enriched garnet cores and decompression textures, although the prograde and retrograde evolution is not constrained quantitatively. The muscovite and biotite breakdown–dehydration reactions for the Na_2O – K_2O – FeO – MgO – Al_2O_3 – SiO_2 – H_2O system from Spear *et al.* (1999) are shown for context.

the lack of associated shear zones might be explained by its greater northward distance from the Bergeron suture (Fig. 2). Considering that the overall kinematics of the THO terminal collision were north-to-south in the Quebec–Baffin segment, it is possible that the south-vergent, late-orogenic F_3 folds developed during the THO terminal collision.

Implications for tectonic processes in large, hot orogens

The Hall Peninsula crustal section records *c.* 25 Myr of crustal shortening and high-grade metamorphism; U–Pb titanite ages (*c.* 1742–1730 Ma; Scott, 1999) suggest that elevated temperatures ($>550^{\circ}\text{C}$) persisted for at least *c.* 95 Myr after the thermal peak. Maximum pressures of $\sim 6.1\text{--}7.35$ kbar estimated using phase diagram models correspond to mid-crustal depths of $\sim 20\text{--}25$ km, based on an assumed crustal density of 2700 kg m^{-3} . Teleseismic profiles through southern Baffin Island indicate a Moho depth of 35–46 km (Snyder, 2010).

Assuming that the area was underlain by the same crustal material as it is now, the crust reached a maximum thickness of at least 55–71 km, similar to the estimated maximum thicknesses in the Grenville (Mezger *et al.*, 1991) and Himalayan orogens (Tiwari *et al.*, 2006). Elevated temperatures over *c.* 100 Myr and crustal thickening on Hall Peninsula are in accordance with the THO as a large, hot, long-duration orogen (e.g. Beaumont *et al.*, 2006). However, the detailed tectono-thermal evolution documented here highlights some differences that set the THO apart from the Grenville and Himalayan orogens, and from the similarly hot Variscan orogen.

The Himalayan orogen exhibits subhorizontal ductile flow of melt-weakened mid-crust in a channel between a thrust-sense lower boundary and a normal-sense upper boundary (e.g. Grujic *et al.*, 2002; Beaumont *et al.*, 2006). Although evidence for similar mid-crustal flow in the Grenville is equivocal, several hallmarks have been recognized in the hinterland, including subhorizontal fabrics and possible shear zones bounding a mid-crustal channel (Rivers, 2008, and references therein). In the Variscan, subhorizontal fabrics and thermal re-equilibration record the lateral flow of the mid-to lower crust in response to the indentation of a continental block into the orogenic root (Schulmann *et al.*, 2008). In contrast to subhorizontal fabrics in the mid-crust of comparable orogens, the regional metamorphic foliation (S_1) in the study area is moderately dipping. Although we cannot rule out the possibility that S_1 was originally subhorizontal prior to D_2 , there is insufficient evidence of lateral flow in a channel structure. There are no known regional structures or bounding shear zones that may indicate channel flow in the THO (St-Onge *et al.*, 2006), suggesting that the necessary rheological conditions were not met, including a laterally continuous layer with sufficiently low viscosity bounded by more rigid crust. This has previously been attributed to the lower volume of pelitic lithologies in the THO relative to other large, hot orogens (St-Onge *et al.*, 2006). In addition, the Cumberland Batholith and coeval orthopyroxene-bearing intrusions in the study area mostly pre-date the main phase of compression between *c.* 1850 and 1825 Ma. Even if not fully crystallized, the dominantly granitic intrusions may have contributed to the rheological heterogeneity of the mid-crust, impeding the development of a laterally continuous, flowing layer.

Collapse in the Grenville orogen is manifested by normal-sense shear zones extending >25 km into the mid-crust (Mezger *et al.*, 1991; Rivers, 2008), rapid exhumation and cooling (Cosca *et al.*, 1992; Busch *et al.*, 1997; Schneider *et al.*, 2013). Rivers (2008) suggested a form of ductile flow beneath an orogenic plateau, followed by collapse once compressive stresses ceased and reworking of the former channel as a normal-sense detachment system. In contrast, no normal-sense faults are recognized in the eastern MIM. U–Pb titanite ages of *c.* 1742–1730 Ma (Scott, 1999) may suggest that

temperatures remained above $\sim 550^{\circ}\text{C}$ (Cherniak, 1993; Hawkins & Bowring, 1999) for ~ 100 Myr after the thermal peak. Muscovite ^{40}Ar – ^{39}Ar ages of c. 1690–1657 Ma may imply that the study area remained hotter than ~ 420 – 450°C (Harrison *et al.*, 2009) for at least 140 Myr post-thermal peak (Skipton *et al.*, 2015). K–Ar ages of muscovite (c. 1610 Ma; Lowdon, 1960), hornblende (c. 1670 Ma; Wanless *et al.*, 1979) and biotite (c. 1700–1507 Ma; Wanless *et al.*, 1968), although variable, also support prolonged high temperatures. Thorough investigation of the cooling history requires more comprehensive thermochronological data and thermal modeling, but the available data suggest slow cooling. Similarly slow cooling rates and the absence of extensional tectonics are characteristic of the THO and particularly the Quebec–Baffin segment (Wanless, 1970; Corrigan *et al.*, 2009).

CONCLUSIONS

1. Field observations, petrography, mineral chemistry, equilibrium phase diagram modeling and *in situ* U–Pb monazite geochronology indicate that the dominant regional deformation event in the internal zone of the NE segment of the THO was east-directed crustal shortening (D_1) at c. 1850–1825 Ma, concurrent with the thermal peak of metamorphism, which reached mid-amphibolite-facies conditions of ~ 720 – 740°C and ~ 6.25 – 7.25 kbar in the east, and granulite-facies conditions of ~ 810 – 890°C and ~ 6.10 – 7.35 kbar in the west.
2. Syn- to post-thermal-peak thick-skinned folds and thrusts (D_2) played an important role in crustal thickening and the overall crustal architecture of the eastern MIM by juxtaposing higher grade thrust sheets eastwards over lower grade rocks.
3. Metamorphism and east-directed shortening (D_1 , D_2) from c. 1850 to 1825 Ma represent an accretionary or collisional event in the upper Churchill plate collage of the THO, and potentially Andean margin style subduction of the Narsajuaq arc (or Sugluk block?) beneath the MIM.
4. U–Pb monazite geochronology suggests that the study area was regionally affected by a post-thermal-peak tectonothermal episode at c. 1800 Ma. Monazite formation was probably due to fluid-assisted dissolution–reprecipitation and appears concomitant with retrograde muscovite growth and south-directed crustal shortening (D_3).
5. The c. 1800 Ma event recorded on Hall Peninsula is synchronous with the terminal collision of the THO at c. 1820–1795 Ma, when the lower plate Superior craton collided with the upper Churchill plate.
6. Significant crustal thickening and elevated temperatures for c. 100 Myr on Hall Peninsula are consistent with the THO being a large, hot, long-duration orogen; however, mid-crustal ductile (channel) flow or orogenic collapse features have not been identified.

ACKNOWLEDGEMENTS

We thank D. Mate and H. Steenkamp of the Canada–Nunavut Geoscience Office (CNGO) for their unwavering scientific and logistical support of this project. The Hall Peninsula Integrated Geoscience Project (HPIGP) team is thanked for their enthusiastic and high-quality field mapping and for many valuable discussions. In particular, this paper benefited from discussions with H. Steenkamp, G. Machado, N. Rayner, M. Young, A. Camacho, B. Dyck, R. From, C. MacKay and Z. Braden. We thank G. Poirier for his assistance in the acquisition of electron microprobe data and SEM images, and Y. Luo for her help in acquiring LA-ICP-MS ages. Thanks are extended to O. Weller for reviewing an earlier version of this paper and for several helpful discussions. K. Dorfler, V. Gardien, J. Majka and an anonymous reviewer are thanked for thorough reviews that helped clarify the arguments presented in this paper. This is Earth Sciences Sector Contribution number 20150310.

FUNDING

This work was funded by the CNGO, HPIGP and additional support was provided by National Science and Engineering Research Council grants to D.A.S. and D.R.S.

SUPPLEMENTARY DATA

Supplementary data for this paper are available at *Journal of Petrology* online.

REFERENCES

- Ashworth, J. R. (1975). The sillimanite zone of the Huntly–Portsoy area in the north-east Dalradian, Scotland. *Geological Magazine* **112**, 113–136.
- Beaumont, C., Nguyen, M. H., Jamieson, R. A. & Ellis, S. (2006). Crustal flow modes in large hot orogens. In: Law, R. D., Searle, M. P. & Godin, L. (eds) *Channel Flow, Ductile Extrusion and Exhumation in Continental Collision Zones*. Geological Society, London, Special Publications **268**, 91–145.
- Bhattacharya, S. (1993). Refinement of geothermobarometry for cordierite granulites. *Proceedings of the Indian Academy of Sciences—Earth and Planetary Sciences* **102**, 537–545.
- Blackadar, R. G. (1967). *Geological reconnaissance, southern Baffin Island, District of Franklin*. Geological Survey of Canada, Paper 6647.
- Brown, M. (1994). The generation, segregation, ascent and emplacement of granite magma: the migmatite-to-crustally derived granite connection in thickened orogens. *Earth–Science Reviews* **36**, 83–130.
- Brown, M. (2004). The mechanism of melt extraction from lower continental crust of orogens. *Transactions of the Royal Society of Edinburgh: Earth Sciences* **95**, 35–48, doi:10.1017/S0263593300000900.
- Brown, M. (2006). Duality of thermal regimes is the distinctive characteristic of plate tectonics since the Neoproterozoic. *Geology* **34**, 961–964.

- Busch, J. P., Mezger, K. & van der Pluijm, B. A. (1997). Suturing and extensional reactivation in the Grenville orogen, Canada. *Geology* **25**, 507–510.
- Chadwick, T. C., St-Onge, M. R., Weller, O. M., Carr, S. D. & Dyck, B. J. (2015). Ptarmigan Fiord basement–cover thrust imbricates, Baffin Island, Nunavut. In: *Summary of Activities 2015*. Iqaluit, NU: Canada-Nunavut Geoscience Office, pp. 61–72.
- Cherniak, D. J. (1993). Pb diffusion in titanite and preliminary results on the effects of radiation damage on Pb transport. *Chemical Geology* **110**, 177–194.
- Chernoff, C. & Carlson, W. D. (1997). Disequilibrium for Ca during growth of pelitic garnet. *Journal of Metamorphic Geology* **15**, 421–438.
- Clark, C., Fitzsimons, I. C. W., Healy, D. & Harley, S. L. (2011). How does the continental crust get really hot? *Elements* **7**, 235–240, doi:10.2113/gselements.7.4.235.
- Corrigan, D., Pehrsson, S., Wodicka, N. & de Kemp, E. (2009). The Palaeoproterozoic Trans-Hudson Orogen: a prototype of modern accretionary processes. In: Murphy, J. B., Keppie, J. D. & Hynes, A. J. (eds) *Ancient Orogens and Modern Analogues*. Geological Society, London, *Special Publications* **327**, 457–479.
- Cosca, M. A., Essene, E. J., Kunk, M. J. & Sutter, J. F. (1992). Differential unroofing within the Central Metasedimentary Belt of the Grenville Orogen: constraints from $^{40}\text{Ar}/^{39}\text{Ar}$ thermochronology. *Contributions to Mineralogy and Petrology* **110**, 211–225.
- De Capitani, C. & Brown, T. H. (1987). The computation of chemical equilibrium in complex systems containing nonideal solutions. *Geochimica et Cosmochimica Acta* **51**, 2639–2652.
- De Capitani, C. & Petrakakis, K. (2010). The computation of equilibrium assemblage diagrams with Theriak/Domino software. *American Mineralogist* **95**, 1006–1016.
- Dyck, B. J. & St-Onge, M. R. (2014). Dehydration-melting reactions, leucogranite emplacement and the Paleoproterozoic structural evolution of Hall Peninsula, Baffin Island, Nunavut. In: *Summary of Activities 2013*. Iqaluit, NU: Canada-Nunavut Geoscience Office, pp. 73–84.
- England, P. C. & Thompson, A. B. (1984). Pressure–temperature–time paths of regional metamorphism: I, Heat transfer during the evolution of regions of thickened continental crust. *Journal of Petrology* **25**, 894–928.
- Evans, B. W. & Guidotti, C. V. (1966). The sillimanite–potash feldspar isograd in Western Maine, U.S.A. *Contributions to Mineralogy and Petrology* **12**, 25–62.
- Florence, F. P. & Spear, F. S. (1991). Effects of diffusional modification of garnet growth zoning on P – T calculations. *Contributions to Mineralogy and Petrology* **107**, 487–500.
- Florence, F. P. & Spear, F. S. (1993). Influences of reaction history and chemical diffusion on P – T calculations for staurolite schists from the Littleton Formation, northwestern New Hampshire. *American Mineralogist* **78**, 345–359.
- Foster, G., Gibson, H. D., Parrish, R. R., Horstwood, M., Fraser, J. & Tindle, A. (2002). Textural, chemical and isotopic insights into the nature and behaviour of metamorphic monazite. *Chemical Geology* **191**, 183–207.
- From, R. E., St-Onge, M. R. & Camacho, A. L. (2014). Preliminary characterization of the Archean orthogneiss complex of Hall Peninsula, Baffin Island, Nunavut. In: *Summary of Activities 2013*. Iqaluit, NU: Canada-Nunavut Geoscience Office, pp. 53–62.
- Gardien, V., Thompson, A. B., Grujic, G. & Ulmer, P. (1995). Experimental melting of biotite + plagioclase + quartz \pm muscovite assemblages and implications for crustal melting. *Journal of Geophysical Research* **100**, 15581–15591.
- Grujic, D., Hollister, L. & Parrish, R. (2002). Himalayan metamorphic sequence as an orogenic channel: insight from Bhutan. *Earth and Planetary Science Letters* **198**, 177–191.
- Guilmette, C., Indares, A. & Hébert, R. (2011). High-pressure anatectic paragneisses from the Namche Barwa, Eastern Himalayan Syntaxis: Textural evidence for partial melting, phase equilibria modeling and tectonic implications. *Lithos* **124**, 66–81.
- Harlov, D. E. & Hetherington, C. J. (2010). Partial high-grade alteration of monazite using alkali-bearing fluids: Experiment and nature. *American Mineralogist* **95**, 1105–1108.
- Harrison, M. T., Célérier, J., Aikman, A. B., Hermann, J. & Heizler, M. T. (2009). Diffusion of ^{40}Ar in muscovite. *Geochimica et Cosmochimica Acta* **73**, 1039–1051.
- Hawkins, D. P. & Bowring, S. A. (1999). U–Pb monazite, xenotime and titanite geochronological constraints on the prograde to post-peak metamorphic thermal history of Paleoproterozoic migmatites from the Grand Canyon, Arizona. *Contributions to Mineralogy and Petrology* **134**, 150–169.
- Henry, D. J., Guidotti, C. V. & Thomson, J. A. (2005). The Ti-saturation surface for low-to-medium pressure metapelitic biotites: implications for geothermometry and Ti-substitution mechanisms. *American Mineralogist* **90**, 316–328.
- Hoffman, P. F. (1988). United Plates of America, the birth of a craton: Early Proterozoic assembly and growth of Laurentia. *Annual Review of Earth and Planetary Sciences* **16**, 543–603.
- Hoffman, P. F. (1990). Dynamics of the assembly of northeast Laurentia in geon 18 (1.9–1.8 Ga). *Geoscience Canada* **17**, 222–226.
- Holland, T. J. B. & Powell, R. (1998). An internally consistent thermodynamic data set for phases of petrological interest. *Journal of Metamorphic Geology* **16**, 309–343.
- Holcombe, R. J. (2009). GEORient. <http://www.holcombe.net.au/software/georient.html>.
- Indares, A., White, R. W. & Powell, R. (2008). Phase equilibria modelling of kyanite-bearing anatectic paragneisses from the central Grenville Province. *Journal of Metamorphic Geology* **26**, 815–836.
- Jackson, G. D., Hunt, P. A., Loveridge, W. D. & Parrish, R. R. (1990). Reconnaissance geochronology of Baffin Island, N.W.T. Radiogenic age and isotopic studies: Report 3, *Geological Survey of Canada, Paper* **89-2**, 123–148.
- Jamieson, R. A., Beaumont, C., Fullsack, P. & Lee, B. (1998). Barrovian regional metamorphism: where's the heat?. In: Treloar, P. J. & O'Brien, P. J. (eds) *What Drives Metamorphism and Metamorphic Reactions?* Geological Society, London, *Special Publications*, **138**, 23–51.
- Kohn, M. J. & Spear, F. (2000). Retrograde net transfer reaction insurance for pressure–temperature estimates. *Geology* **28**, 1127–1130.
- LeBreton, N. & Thompson, A. B. (1988). Fluid-absent (dehydration) melting of biotite in pelites in the early stages of crustal anatexis. *Contributions to Mineralogy and Petrology* **99**, 226–237.
- Lewry, J. F. & Collerson, K. D. (1990). The Trans-Hudson Orogen: extent, subdivisions and problems. In: Lewry, J. F. & Stauffer, M. R. (eds) *The Early Proterozoic Trans-Hudson Orogen of North America*. Geological Association of Canada, *Special Paper* **37**, 1–14.
- Lowdon, J. A. (1960). Age determinations by the Geological Survey of Canada, Report 1—isotopic ages. *Geological Survey of Canada, Paper* **60-17**, 5–40.
- Lucas, S. B. (1989). Structural evolution of the Cape Smith thrust belt, and the role of out-of-sequence faulting in the thickening of mountain belts. *Tectonics* **8**, 655–676.
- Ludwig, K. (2003). *User's Manual for Isoplot/Ex rev. 3.00: a Geochronological Toolkit for Microsoft Excel*. Berkeley Geochronology Center Special Publications **4**.

- Machado, G., Bilodeau, C. & St-Onge, M. R. (2013). Geology, southern part of Hall Peninsula, south Baffin Island, Nunavut, Geological Survey of Canada Canadian Geoscience Map 135 (preliminary). Iqaluit, NU: Canada-Nunavut Geoscience Office, Open File Map 2013-1, scale 1:250 000, doi:10.4095/292443.
- MacKay, C. B. & Ansdell, K. M. (2014). Geochemical study of mafic and ultramafic rocks from southern Hall Peninsula, Baffin Island, Nunavut. In: *Summary of Activities 2013*. Iqaluit, NU: Canada-Nunavut Geoscience Office, pp. 85–92.
- Mahan, K. H., Goncalves, P., Williams, M. L. & Jercinovic, M. J. (2006). Dating metamorphic reactions and fluid flow: application to exhumation of high-*P* granulites in a crustal-scale shear zone, western Canadian Shield. *Journal of Metamorphic Geology* **24**, 193–217.
- Mezger, K., Van Der Pluijm, B. A., Essene, E. J. & Halliday, A. N. (1991). Synorogenic collapse: A perspective from the middle crust, the Proterozoic Grenville Orogen. *Science* **254**, 695–698.
- Palin, R. M., Searle, M. P., St-Onge, M. R., Waters, D. J., Roberts, N. M. W., Horstwood, M. S. A., Parrish, R. R., Weller, O. M., Chen, S. & Yang, J. (2014). Monazite geochronology and petrology of kyanite- and sillimanite-grade migmatites from the northwestern flank of the eastern Himalayan syntaxis. *Gondwana Research* **26**, 323–347.
- Patiño Douce, A. E. & Johnston, A. D. (1991). Phase equilibria and melt productivity in the pelitic system: implications for the origin of peraluminous granulites and aluminous granulites. *Contributions to Mineralogy and Petrology* **107**, 202–218.
- Powell, R. & Holland, T. J. B. (2008). On thermobarometry. *Journal of Metamorphic Geology* **26**, 155–179.
- Pyle, J. M. & Spear, F. S. (1999). Yttrium zoning in garnet: coupling of major and accessory phases during metamorphic reactions. *Geological Materials Research* **1**, 1–49.
- Pyle, J. M. & Spear, F. S. (2003). Four generations of accessory-phase growth in low-pressure migmatites from SW New Hampshire. *American Mineralogist* **88**, 338–351.
- Rayner, N. M. (2014). New U–Pb geochronological results from Hall Peninsula, Baffin Island, Nunavut. In: *Summary of Activities 2013*. Iqaluit, NU: Canada-Nunavut Geoscience Office, pp. 39–52.
- Rayner, N. M. (2015). New (2013–2014) U–Pb geochronological results from northern Hall Peninsula, southern Baffin Island, Nunavut. In: *Summary of Activities 2014*. Iqaluit, NU: Canada-Nunavut Geoscience Office, pp. 31–44.
- Rivers, T. (2008). Assembly and preservation of lower, mid, and upper orogenic crust in the Grenville Province—Implications for the evolution of large hot long-duration orogens. *Precambrian Research* **167**, 237–259.
- Sawyer, E. W. (1999). Criteria for the recognition of partial melting. *Physics and Chemistry of the Earth (A)* **24**, 269–279.
- Schneider, D. A., Cope, N. & Holm, D. K. (2013). Thermochronology of the Mont Laurier terrane, southern Canadian Grenville Province, and its bearing on defining orogenic architecture. *Precambrian Research* **226**, 43–58.
- Schulmann, K., Lexa, O., Stipská, P., Racek, M., Tajčmanová, L., Konopásek, J., Edel, J.-B., Peschler, A. & Lehmann, J. (2008). Vertical extrusion and horizontal channel flow of orogenic lower crust: key exhumation mechanisms in large hot orogens?. *Journal of Metamorphic Geology* **26**, 273–297.
- Scott, D. J. (1999). U–Pb geochronology of the eastern Hall Peninsula, southern Baffin Island, Canada: a northern link between the Archean of West Greenland and the Paleoproterozoic Torngat Orogen of northern Labrador. *Precambrian Research* **93**, 5–26.
- Scott, D. J. & Gauthier, G. (1996). Comparison of TIMS (U–Pb) and laser ablation microprobe ICP-MS (Pb) techniques for age determination of detrital zircons from Paleoproterozoic metasedimentary rocks from northeastern Laurentia, Canada, with tectonic implications. *Chemical Geology* **131**, 127–142.
- Scott, D. J. & Wodicka, N. (1998). A second report on the U–Pb geochronology of southern Baffin Island. *Geological Survey of Canada, Paper* **1998-F**, 47–57.
- Seydoux-Guillaume, A.-M., Paquette, J. L., Wiedenbeck, M., Montel, J.-M. & Heinrich, W. (2002). Experimental resetting of the U–Th–Pb systems in monazite. *Chemical Geology* **191**, 165–181.
- Skipton, D. R. & St-Onge, M. R. (2014). Paleoproterozoic deformation and metamorphism in metasedimentary rocks west of Okalik Bay: a field template for the evolution of eastern Hall Peninsula, Baffin Island, Nunavut. In: *Summary of Activities 2013*. Iqaluit, NU: Canada-Nunavut Geoscience Office, pp. 63–72.
- Skipton, D. R., Schneider, D. A., Kellett, D. & Joyce, N. (2015). New insights on the cooling history of Hall Peninsula, southern Baffin Island, Nunavut, using $^{40}\text{Ar}/^{39}\text{Ar}$ thermochronology on muscovite. In: *Summary of Activities 2014*. Iqaluit, NU: Canada-Nunavut Geoscience Office, pp. 17–30.
- Snyder, D. B. (2010). Mantle lithosphere structure beneath southeast Baffin Island, Nunavut, from teleseismic studies. *Geological Survey of Canada, Current Research* **2010-8**, 6 pp.
- Spear, F. S. (2004). Fast cooling and exhumation of the Valhalla metamorphic core complex, southeastern British Columbia. *International Geology Review* **46**, 193–209.
- Spear, F. S. & Parrish, R. R. (1996). Petrology and cooling rates of the Valhalla complex, British Columbia, Canada. *Journal of Petrology* **37**, 733–765.
- Spear, F. S. & Pyle, J. M. (2010). Theoretical modeling of monazite growth in a low-Ca metapelite. *Chemical Geology* **273**, 111–119.
- Spear, F. S., Kohn, M. J., Florence, F. P. & Menard, T. (1990). A model for garnet and plagioclase growth in pelitic schists: implications for thermobarometry and *P–T* path determinations. *Journal of Metamorphic Geology* **8**, 683–696.
- Spear, F. S., Kohn, M. J. & Cheney, J. T. (1999). *P–T* paths from anatectic pelites. *Contributions to Mineralogy and Petrology* **134**, 17–32.
- Steenkamp, H. M. & St-Onge, M. R. (2014). Overview of the 2013 regional bedrock mapping program on northern Hall Peninsula, Baffin Island, Nunavut. In: *Summary of Activities 2013*. Iqaluit, NU: Canada-Nunavut Geoscience Office, pp. 27–38.
- St-Onge, M. R. (1987). Zoned poikiloblastic garnets: *P–T* paths and syn-metamorphic uplift through 30 km of structural depth, Wopmay Orogen, Canada. *Journal of Petrology* **28**, 1–21.
- St-Onge, M. R., Scott, D. J. & Lucas, S. B. (2000). Early partitioning of Quebec: microcontinent formation in the Paleoproterozoic. *Geology* **28**, 323–326.
- St-Onge, M. R., Searle, M. P. & Wodicka, N. (2006). Trans-Hudson Orogen of North America and Himalaya–Karakorum–Tibetan Orogen of Asia: structural and thermal characteristics of the lower and upper plates. *Tectonics* **25**, 1–22, doi:10.1029/2005TC001907.
- St-Onge, M. R., Wodicka, N. & Ijwiliw, O. (2007). Polymetamorphic evolution of the Trans-Hudson Orogen, Baffin Island, Canada: integration of petrological, structural and geochronological data. *Journal of Petrology* **48**, 271–302.

- St-Onge, M. R., Van Gool, J. A. M., Garde, A. A. & Scott, D. J. (2009). Correlation of Archaean and Palaeoproterozoic units between northeastern Canada and western Greenland: constraining the pre-collisional upper plate accretionary history of the Trans-Hudson Orogen. In: Cawood, P. A. & Kröner, A. (eds) *Earth Accretionary Systems in Space and Time. Geological Society, London, Special Publication* **318**, 193–235.
- Thériault, R. J., St-Onge, M. R. & Scott, D. J. (2001). Nd isotopic and geochemical signature of the Paleoproterozoic Trans-Hudson Orogen, southern Baffin Island, Canada: implications for the evolution of eastern Laurentia. *Precambrian Research* **108**, 113–138.
- Tiwari, V. M., Vyghreswara Rao, M. B. S., Mishra, D. C. & Singh, B. (2006). Crustal structure across Sikkim, NE Himalaya from new gravity and magnetic data. *Earth and Planetary Science Letters* **247**, 61–69.
- Tyler, I. M. & Ashworth, J. R. (1982). Sillimanite–potash feldspar assemblages in graphitic pelites, Strontian Island, Scotland. *Contributions to Mineralogy and Petrology* **81**, 18–29.
- Vernon, R. H. & Ransom, D. M. (1971). Retrograde schists of the amphibolite facies at Broken Hill, New South Wales. *Journal of the Geological Society of Australia* **18**, 267–277.
- Wanless, R. K. (1970). Isotopic age map of Canada. Geological Survey of Canada, 'A' Series Map 1265 A, doi:10.4095/108982.
- Wanless, R. K., Stevens, R. D., Lachance, G. R. & Edmonds, C. M. (1968). Age determinations and geological studies. In: K–Ar isotopic ages, *Report 8. Geological Survey of Canada, Paper* **67-2 A**, 11–141.
- Wanless, R. K., Stevens, R. D., Lachance, G. R. & Delabio, R. N. (1979). Age determinations and geological studies. In: K–Ar isotopic ages, *Report 14. Geological Survey of Canada, Paper* **79-2**, 167.
- Wawrzenitz, N., Krohe, A., Rhede, D. & Romer, R. L. (2012). Dating rock deformation with monazite: The impact of dissolution precipitation creep. *Lithos* **134–135**, 52–74.
- Weller, O. M., St-Onge, M. R., Waters, D. J., Rayner, N., Searle, M. P., Chung, S.-L., Palin, R. M., Lee, Y.-H. & Xu, X. (2013). Quantifying Barrovian metamorphism in the Danba Structural Culmination of eastern Tibet. *Journal of Metamorphic Geology* **31**, 909–935.
- Whalen, J. B., Wodicka, N., Taylor, B. E. & Jackson, G. D. (2010). Cumberland Batholith, Trans-Hudson Orogen, Canada: Petrogenesis and implications for Paleoproterozoic crustal and orogenic processes. *Lithos* **117**, 99–118.
- White, R. W., Powell, R. & Holland, T. J. B. (2001). Calculation of partial melting equilibria in the system Na₂O–CaO–FeO–MgO–Al₂O₃–SiO₂–H₂O (NCKFMASH). *Journal of Metamorphic Geology* **19**, 139–153.
- Williams, M. L., Jercinovic, M. J., Harlov, D. E., Budzyń, B. & Hetherington, C. J. (2011). Resetting monazite ages during fluid-related alteration. *Chemical Geology* **283**, 218–225.
- Wodicka, N. & Scott, D. J. (1997). A preliminary report on the U–Pb geochronology of the Meta Incognita Peninsula, southern Baffin Island, Northwest Territories. *Geological Survey of Canada, Paper* **1997-C**, 167–178.
- Woodsworth, G. J. (1977). Homogenization of zoned garnets from pelitic schists. *Canadian Mineralogist* **15**, 230–242.